

ZoomNeXt: A Unified Collaborative Pyramid Network for Camouflaged Object Detection

Youwei Pang^{1*}, Xiaoqi Zhao^{1*}, Tian-Zhu Xiang^{2*},
Lihe Zhang, *Member, IEEE*^{1†}, and Huchuan Lu, *Fellow, IEEE*¹

¹Dalian University of Technology, China, ²Inception Institute of Artificial Intelligence and G42, UAE

<https://github.com/lartpang/ZoomNeXt>

Abstract

Recent camouflaged object detection (COD) attempts to segment objects visually blended into their surroundings, which is extremely complex and difficult in real-world scenarios. Apart from the high intrinsic similarity between camouflaged objects and their background, objects are usually diverse in scale, fuzzy in appearance, and even severely occluded. To this end, we propose an effective unified collaborative pyramid network that mimics human behavior when observing vague images and videos, *i.e.*, zooming in and out. Specifically, our approach employs the zooming strategy to learn discriminative mixed-scale semantics by the multi-head scale integration and rich granularity perception units, which are designed to fully explore imperceptible clues between candidate objects and background surroundings. The former’s intrinsic multi-head aggregation provides more diverse visual patterns. The latter’s routing mechanism can effectively propagate inter-frame differences in spatiotemporal scenarios and be adaptively deactivated and output all-zero results for static representations. They provide a solid foundation for realizing a unified architecture for static and dynamic COD. Moreover, considering the uncertainty and ambiguity derived from indistinguishable textures, we construct a simple yet effective regularization, uncertainty awareness loss, to encourage predictions with higher confidence in candidate regions. Our highly task-friendly framework consistently outperforms existing state-of-the-art methods in image and video COD benchmarks.

Keywords Image Camouflaged Object Detection, Video Camouflaged Object Detection, Image and Video Unified Architecture.

1 Introduction

Camouflaged objects are often “seamlessly” integrated into the environment by changing their appearance, coloration or pattern to avoid detection, such as chameleons, cuttlefishes and flatfishes. This natural defense mechanism has evolved in response to their harsh living environments. Broadly speaking, camouflaged objects also refer to objects that are extremely small in size, highly similar to the background, or heavily obscured. They subtly hide themselves in the surroundings, making them difficult to be found, *e.g.*, soldiers wearing camouflaged uniforms and lions hiding in the grass. Therefore, camouflaged object detection (COD) presents a significantly more intricate challenge compared to traditional

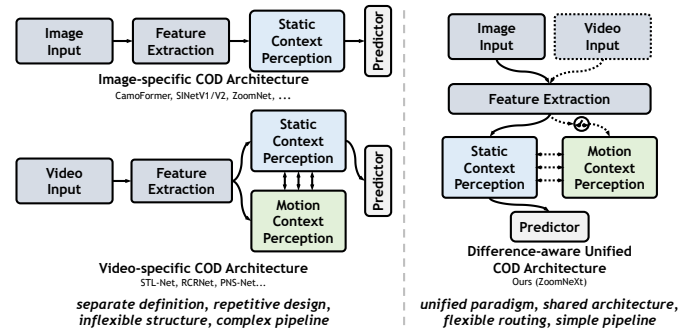


Figure 1: Comparison of the proposed framework with existing paradigms. Existing methods feed the image and video inputs into task-specific architecture to yield camouflaged object map. Unlike them, our ZoomNeXt, which is founded on the flexible difference-aware routing mechanism \odot , unifies and simplifies the processing pipeline of image and video COD tasks, which shares powerful static components without introducing redundant computation.

salient object detection (SOD) or other object segmentation. Recently, it has piqued ever-growing research interest from the computer vision community and facilitates many valuable real-life applications, such as search and rescue [17], species discovery [58], medical analysis (*e.g.*, polyp segmentation [15, 31, 97], lung infection segmentation [16], and cell segmentation [38]), agricultural management [44, 64], and defect detection [4, 18].

Recently, numerous deep learning-based methods have been proposed and achieved significant progress. Nevertheless, they still struggle to accurately and reliably detect camouflaged objects, due to the visual insignificance of camouflaged objects, and high diversity in scale, appearance, and occlusion. By observing our experiments, it is found that the current COD detectors are susceptible to distractors from background surroundings. Thus it is difficult to excavate discriminative and subtle semantic cues for camouflaged objects, resulting in the inability to clearly segment the camouflaged objects from the chaotic background and the predictions of some uncertain (low-confidence) regions. In addition, recent works [6, 9, 35] have attempted to introduce temporal motion cues of objects to further expand the information dimension of the COD task. However, as shown in Fig. 1, the existing best solutions for image [17, 56, 89] and video [9] COD tasks have different information emphases (*i.e.*, the appearance information of static images and the motion information of videos), resulting in incompatibility in architecture design and feature pipeline between the two types of tasks. The task-specific development and evolution bring repetitive exploration, inflexible cross-task structures, redundant parameters, and

*These authors contributed equally to this work.

†Corresponding author.

resource overhead. The unification of the two tasks has a positive value in fully exploiting the inter-task commonalities and leveraging powerful shared components (*e.g.*, feature extraction and static context perception as shown in Fig. 1) to integrate key static cues from the image and video inputs. In addition, it is poorly performed to apply image models to the video field because of the absence of motion perception. And, video models based on the predefined motion information need to specifically compensate for missing auxiliary inputs and bring unnecessary computation when handling static images. Taking these into mind, in this paper, we summarize the COD issue into three aspects: 1) *How to accurately locate camouflaged objects under conditions of inconspicuous appearance and various scales?* 2) *How to design a unified framework that is compatible with both image and video feature processing pipelines?* 3) *How to suppress the obvious interference from the background and infer camouflaged objects more reliably?*

Intuitively, to accurately find the vague or camouflaged objects in the scene, humans may try to refer to and compare the changes in the shape or appearance at different scales by zooming in and out the image or video. This specific behavior pattern of human beings motivates us to identify camouflaged objects by mimicking the zooming in and out strategy. With this inspiration, in this paper, we propose a unified collaborative pyramid network, named *ZoomNeXt*, which significantly improves the existing camouflaged object detection performance for the image and video COD tasks. **Firstly**, for accurate object location, we employ scale space theory [41, 42, 80] to imitate zooming in and out strategy. Specifically, we design two key modules, *i.e.*, the multi-head scale integration unit (MHSIU) and the rich granularity perception unit (RGPU). For the camouflaged object of interest, our model extracts discriminative features at different “zoom” scales using the triplet architecture, then adopts MHSIUs to screen and aggregate scale-specific features, and utilizes RGPUs to further reorganize and enhance mixed-scale features. **Secondly**, the difference-aware adaptive routing mechanism of the module RGPU can also make full use of the inter-frame motion information to capture camouflaged objects in the video. This flexible data-aware architecture design seamlessly unifies the processing pipeline for static images and video clips into a single convolutional model. Thus, our model is able to mine the accurate and subtle semantic clues between objects and backgrounds under mixed scales and diverse scenes, and produce accurate predictions. Besides, the shared weight strategy used in the proposed method achieves a good balance of efficiency and effectiveness. **Thirdly**, the last aspect is related to reliable prediction in complex scenarios. Although the object is accurately located, the indistinguishable texture and background will easily bring negative effects to the model learning, *e.g.*, predicting uncertain/ambiguous regions, which greatly reduces the detection performance and cannot be ignored. This can be seen in Fig. 8 (Row 3 and 4) and Fig. 10. To this end, we design a uncertainty awareness loss (UAL) to guide the model training, which is only based on the prior knowledge that a good COD prediction should have a clear polarization trend. Its characteristic of not relying on ground truth (GT) data makes it suitable for enhancing the GT-based BCE loss. This targeted enhancement strategy can force the network to optimize the prediction of the uncertain

regions during the training process, enabling our *ZoomNeXt* to distinguish the uncertain regions and segment the camouflaged objects reliably.

Our contributions can be summarized as follows:

1. For the COD task, we propose *ZoomNeXt*, which can credibly capture the objects in complex scenes by characterizing and unifying the scale-specific appearance features at different “zoom” scales and the purposeful optimization strategy.
2. To obtain the discriminative feature representation of camouflaged objects, we design MHSIUs and RGPUs to distill, aggregate, and strengthen the scale-specific and subtle semantic representation for accurate COD.
3. Through a carefully-designed difference-aware adaptive routing mechanism, our unified conditional architecture seamlessly combines the image and video feature pipelines, enhancing scalability and flexibility.
4. We propose a simple yet effective optimization enhancement strategy, UAL, which can significantly suppress the uncertainty and interference from the background without increasing extra parameters.
5. Without bells and whistles, our model greatly surpasses the recent 30 state-of-the-art methods on four image and two video COD data benchmarks, respectively.

A preliminary version of this work was published in [56]. In this paper, we extend our conference version in the following aspects. First, we **improve image-specific *ZoomNet* to image-video unified *ZoomNeXt***. We extend the original static image COD framework to enable further compatibility with the new auxiliary video-related temporal cues. Second, we **explore the video COD task**. Based on the improved framework, we extend the targeted task from the single image COD task to image and video COD tasks. Third, we **improve the performance of our method by introducing more structural extensions**, *i.e.*, multi-head scale integration unit and rich granularity perception unit. They make our approach superior not only to the conference version, but even to several recent cutting-edge competitors. Fourth, we also **introduce and discuss more recently published algorithms for image and video tasks** so as to track recent developments in the field and make fair and reasonable comparisons. Last but not least, we **provide more analytical experiments and visualization** to further study the effectiveness and show the characteristics of the provided components in our method including the MHSIU, RGPU, and GT-free loss function UAL, which helps to better understand their behavior.

2 Related Work

2.1 Camouflaged Object Detection (COD)

Before the visual detection of camouflaged objects as objects of interest becomes an independent task in computer vision, research on such objects has a long history in biology [51, 69, 75]. This behavior of creatures in nature can be regarded as the result of natural selection and adaptation. In fact, in human life and other parts of society, it also has a profound impact, *e.g.*, arts, popular culture, and design. In the computer vision field, research on camouflaged objects is often associated with visual

salience analysis [20, 59, 74, 84] based on the mechanism of human visual attention.

Different from the established salient object detection (SOD) [7, 77, 78, 101] task for the general observation paradigm (*i.e.*, finding visually prominent objects), the COD task pays more attention to the undetectable objects (mainly because of too small size, occlusion, concealment or self-disguise). Due to the differences in the attributes of the objects of interest, the goals of the two tasks are different. The difficulty and complexity of the COD task far exceed the SOD task due to the high similarity between the object and the environment [8, 10, 91]. Therefore, it is necessary to establish models based on the essential requirements and specific data of the task to learn the special knowledge. Although it has practical significance in both the image and video fields, the COD task is still a relatively under-explored computer vision problem. Some valuable attempts have been made in recent years. The pioneering works [14, 36, 48] collect and release several important image COD datasets CAMO [36], COD10K [14], and NC4K [48]. And, another vanguard [9] extends the task to the video COD task and introduces a large-scale comprehensive dataset MoCA-Mask [9]. These datasets have become representative data benchmarks for the COD task nowadays and built a solid foundation for a large number of subsequent studies.

Recent works [23, 32, 36, 48, 72, 90, 102] construct the multi-task learning framework in the prediction process of camouflaged objects and introduce some auxiliary tasks like classification, edge detection, and object gradient estimation. Among them, [23] also attempts to address the intrinsic similarity of foreground and background for COD in the frequency domain. Some uncertainty-aware methods [37, 88, 92] are proposed to model and cope with the uncertainty in data annotation or COD data itself. In the other methods [50, 71], contextual feature learning also plays an important role. And [34] introduces an explicit coarse-to-fine detection and iterative refinement strategy to refine the segmentation effect. Compared to convolutional neural networks, the vision transformer can encode global contextual information more effectively and also change the way existing methods [9, 26, 28, 45, 83, 89] perceive contextual information. Specifically, [83, 89] are based on the strategy of dividing and merging foreground and background to accurately distinguish highly similar foreground and background. [9] utilizes the multi-scale correlation aggregation and the spatiotemporal transformer to construct short-term and long-term information interactions, and optimize temporal segmentation. [28] aims to enhance locality modeling of the transformer-based model and the feature aggregation in decoders, while [26] preserves detailed clues through the high-resolution iterative feedback design. In addition, there are also a number of bio-inspired methods, such as [14, 17, 85]. They capture camouflaged objects by imitating the behavior process of hunters or changing the viewpoint of the scene.

Although our method can also be attributed to the bio-inspired paradigm, ours is different from the above methods. Our method simulates the behavior of humans to understand complex images by zooming in and out strategy. The proposed method explores the scale-specific and imperceptible semantic features under the mixed scales for accurate predictions, with the supervision of BCE and

our proposed UAL. At the same time, through the adaptive perception ability of the temporal difference, the proposed method also harmonizes both image and video data in a single framework. Accordingly, our method achieves a more comprehensive understanding of the diverse scene, and accurately and robustly segments the camouflaged objects from the complex background.

2.2 Conditional Computation

Conditional computation [3] refers to a series of carefully constructed algorithms in which each input sample actually uses only a subset of feature processing nodes. It can further reduce computation, latency, or power on average, and increase model capacity without a proportional increase in computation. As argued in [3], *sparse activations* and *multiplicative connections* may be useful ingredients of conditional computation. Over the past few years, it has become an important solution to the time-consuming and computationally expensive training and inference of deep learning models. Specifically, as a typical paradigm, the mixture of experts (MoE) technique [29] based on sparse selection has shown great potential on a variety of different types of tasks, including language modeling and machine translation [66], multi-task learning [22], image classification [47, 63], and vision-language model [67]. Existing methods mainly rely on MoE and gating strategies to realize dynamic routing of feature flow nodes, and focus on the distinction between different samples of homogeneous data. In the proposed scheme, we propose a new form of conditional computation for differentiated processing of image and video data. Specifically, we construct adaptive video-specific bypasses using the inter-frame difference in video, which is driven by the inter-frame motion information and only responsible for perceiving and excavating dynamic cues, and will be adaptively deactivated and output all-zero results when facing the static image. Such a design decouples universal static perception and specific motion perception, resulting in good compatibility across image and video COD tasks.

2.3 Scale Space Integration

The scale-space theory aims to promote an optimal understanding of image structure, which is an extremely effective and theoretically sound framework for addressing naturally occurring scale variations. Its ideas have been widely used in computer vision, including the image pyramid [2, 19] and the feature pyramid [40]. Due to the structural and semantic differences at different scales, the corresponding features play different roles. However, the commonly-used inverted pyramid-like feature extraction structures [24, 62, 96] often cause the feature representation to lose too much texture and appearance details, which are unfavorable for dense prediction tasks [46, 65] that emphasize the integrity of regions and edges. Thus, some recent CNN-based COD methods [14, 50, 71, 90] and SOD methods [5, 27, 33, 43, 54, 55, 94, 95, 98] explore the combination strategy of inter-layer features to enhance the feature representation. These bring some positive gains for accurate localization and segmentation of objects. However, for the COD task, the existing approaches overlook the performance bottleneck caused by the ambiguity of the structural information of the data

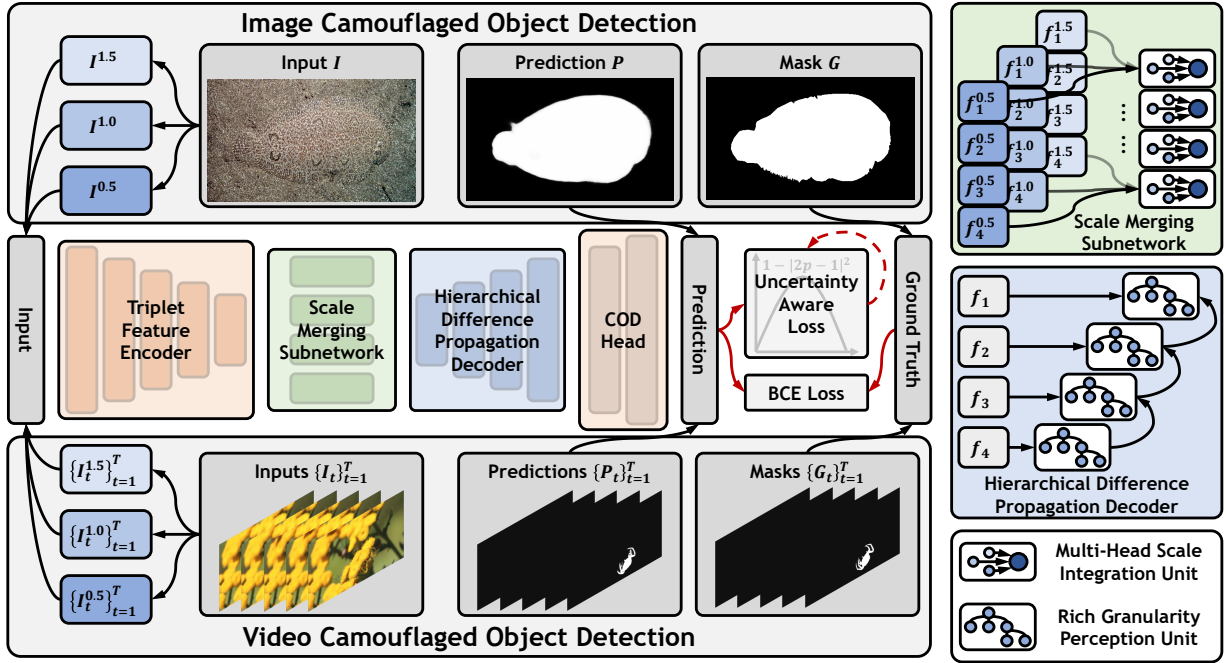


Figure 2: Overall framework of the proposed ZoomNeXt. The shared triplet feature encoder is used to extract multi-level features corresponding to different input “zoom” scales. At different levels of the scale merging subnetwork, MHSIUs are adopted to screen and aggregate the critical cues from different scales. Then the fused features are gradually integrated through the top-down up-sampling path in the hierarchical difference propagation decoder. RGPUs further enhance the feature discrimination by constructing a multi-path structure inside the features. Finally, the probability map of the camouflaged object corresponding to the input image or frame can be obtained. In the training stage, the binary cross entropy and the proposed uncertainty awareness loss are used as the loss function.

itself which makes it difficult to be fully perceived at a single scale. Different from them, we mimic the zoom strategy to synchronously consider differentiated relationships between objects and background at multiple scales, thereby fully perceiving the camouflaged objects and confusing scenes. Besides, we also further explore the fine-grained feature scale space between channels.

3 Method

In this section, we first elaborate on the overall architecture of the proposed method, and then present the details of each module and the uncertainty awareness loss function.

3.1 Overall Architecture

Preliminaries Let $\mathbf{I} \in \mathbb{R}^{3 \times H \times W}$ and $\{\mathbf{I}_t \in \mathbb{R}^{3 \times H \times W}\}_{t=1}^T$ be the input static image and the input video clip with T frames of the network, where 3 is the number of color channels and H, W are the height and width. Our network is to generate a gray-scale map \mathbf{P} or clip $\{\mathbf{P}_t\}_{t=1}^T$ with values ranging from 0 to 1, which reflects the probability that each location may be part of the camouflaged object.

Zooming Strategy The overall architecture of the proposed method is illustrated in Fig. 2. Inspired by the zooming strategy from human beings when observing confusing scenes, we argue that different zoom scales often contain their specific information. Aggregating the differentiated information on different scales will benefit exploring the inconspicuous yet valuable clues from confusing scenarios, thus facilitating COD. To implement it, intuitively, we resort to the image pyramid. Specifically, we customize an image pyramid based on the single scale

input to identify the camouflaged objects. The scales are divided into a main scale (*i.e.*, the input scale) and two auxiliary scales. The latter is obtained by re-scaling the input to imitate the operation of zooming in and out.

Feature Processing We utilize the shared triplet feature encoder to extract features on different scales and feed them to the scale merging subnetwork. To integrate these features that contain rich scale-specific information, we design a series of multi-head scale integration units (MHSIUs) based on the attention-aware filtering mechanism. Thus, these auxiliary scales are integrated into the main scale, *i.e.*, information aggregation of the “zoom in and out” operation. This will largely enhance the model to distill critical and informative semantic cues for capturing difficult-to-detect camouflaged objects. After that, we construct rich granularity perception units (RGPUs) to gradually integrate multi-level features in a top-down manner to enhance the mixed-scale feature representation. It further increases the receptive field range and diversifies feature representation within the module. The captured fine-grained and mixed-scale clues promote the model to accurately segment the camouflaged objects in the chaotic scenes.

Loss Improvement To overcome the uncertainty in the prediction caused by the inherent complexity of the data, we design an uncertainty awareness loss (UAL) to assist the BCE loss, enabling the model to distinguish these uncertain regions and produce an accurate and reliable prediction.

3.2 Triplet Feature Encoder

We start by extracting deep features through a shared triplet feature encoder for the group-wise inputs, which consists of a feature extraction network and a channel compression network. The feature extraction network

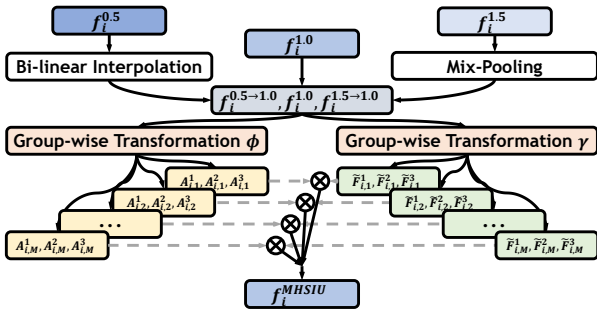


Figure 3: Illustration of the multi-head scale integration unit. \otimes is the element-wise multiplication. ϕ and γ are the parameters of the two separated group-wise transformation layers. More details can be found in Sec. 3.3.

is constituted by the commonly-used ResNet [25], EfficientNet [73], or PVTv2 [79] that removes the classification head. And the channel compression network is cascaded to further optimize computation and obtain a more compact feature. For the trade-off between efficiency and effectiveness, the main scale and the two auxiliary scales are empirically set to $1.0\times$, $1.5\times$, and $0.5\times$. And, three sets of 64-channel feature maps corresponding to three input scales are produced by these structures, *i.e.*, $\{f_i^k\}_{i=1}^5$, $k \in \{0.5, 1.0, 1.5\}$. Next, these features are fed successively to the multi-head scale merging subnetwork and the hierarchical difference propagation decoder for subsequent processing.

3.3 Scale Merging Subnetwork

We design an attention-based multi-head scale integration unit (MHSIU) to screen (weight) and combine scale-specific information, as shown in Fig. 3. Several such units make up the scale merging subnetwork. Through filtering and aggregation, the expression of different scales is self-adaptively highlighted. This component is described in detail next.

Scale Alignment Before scale integration, the features $f_i^{1.5}$ and $f_i^{0.5}$ are first resized to be consistent resolution with the main scale feature $f_i^{1.0}$. Specifically, for $f_i^{1.5}$, we use a hybrid structure of “max-pooling + average-pooling” inspired by [81] to down-sample it, which helps to preserve the effective and diverse responses for camouflaged objects in high-resolution features. For $f_i^{0.5}$, we directly up-sample it by the bi-linear interpolation. Then, these features are fed into the subsequent transformation layers.

Multi-Head Spatial Interaction Unlike the form of spatial attention in our conference version [56] that relies heavily on a single pattern, here we perform parallel independent transformations on M groups of feature maps, which is inspired by the structure of the multi-head paradigm in Transformer [76]. This design helps extend the model’s ability to mine multiple fine-grained spatial attention patterns in parallel and diversify the representation of the feature space. Specifically, several three-channel feature maps are calculated through a series of convolutional layers. After the cascaded softmax activation layer in each attention group, the attention map A_m^k corresponding to each scale can be obtained from these groups and used as respective weights for the final integration, where scale group index $k \in \{1, 2, 3\}$ and attention group index $m \in \{1, 2, \dots, M\}$. The process is

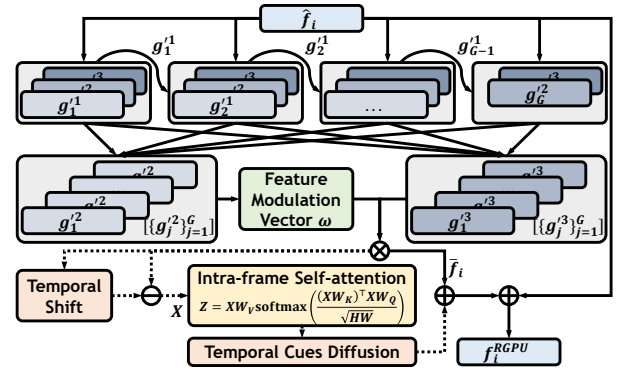


Figure 4: Rich granularity perception unit where \otimes , \oplus , and \ominus are the element-wise multiplication, addition, and subtraction. Group-wise interaction and channel-wise modulation are used to explore the discriminative and valuable semantics from different channels. Each feature group is executed sequentially and the latter one integrates part of the features of the previous one before the feature transformation. The temporal shifting operation shifts the frame feature maps along the temporal dimension and some temporal convolutional layers diffuse the temporal cues as stated in Sec. 3.4.

formulated as:

$$\begin{aligned}
 F_i &= [\mathcal{U}(f_i^{0.5}), f_i^{1.0}, \mathcal{D}(f_i^{1.5})], \\
 \hat{F}_i &= \{\text{trans}(F_i, \phi^m)\}_{m=1}^M, \\
 A_i &= \{\text{softmax}(\hat{F}_{i,m})\}_{m=1}^M, \\
 \tilde{F}_i &= \{\text{trans}(F_i, \gamma^m)\}_{m=1}^M, \\
 f_i^{MHSIU} &= \{A_{i,m}^1 \otimes \tilde{F}_{i,m}^1 + A_{i,m}^2 \otimes \tilde{F}_{i,m}^2 + A_{i,m}^3 \otimes \tilde{F}_{i,m}^3\}_{m=1}^M,
 \end{aligned} \tag{1}$$

where $[\star]$ represents the concatenation operation. \mathcal{U} and \mathcal{D} refer to the bi-linear interpolation and hybrid adaptive pooling operations mentioned above, respectively. $\text{trans}(\star, \phi)$ and $\text{trans}(\star, \gamma)$ indicate the several simple linear transformation layers with the parameters ϕ and γ in the attention generator. And \otimes is the element-wise multiplication operation. Note that some linear, normalization, and activation layers are not shown in Equ. 1 and Fig. 3 for simplicity. And features enhanced in different groups are concatenated along the channel dimension and fed into a decoder for further processing. These designs aim to adaptively and selectively aggregate the scale-specific information to explore subtle but critical semantic cues at different scales, boosting the feature representation.

3.4 Hierarchical Difference Propagation Decoder

After MHSIUs, the auxiliary-scale information is integrated into the main-scale branch. Similar to the multi-scale case, different channels also contain differentiated semantics. Thus, it is necessary to excavate valuable clues contained in different channels. To this end, we design the rich granularity perception unit (RGPU) to conduct information interaction and feature refinement between channels, which strengthen features from coarse-grained group-wise iteration to fine-grained channel-wise modulation in the decoder, as depicted in Fig. 4.

Input The input \hat{f}_i of the $RGPU_i$ contains the multi-scale fused feature f_i^{MHSIU} from the $MHSIU_i$ and the feature

Algorithm 1: The iteration process in the RGPU.

Input: $\{g_j\}_{j=1}^G$: feature groups; $G \geq 2$: the number of groups;
 $\text{CBR}_{C_o \times C_i}$: “ $3 \times 3 \text{Conv-BN-ReLU}$ ” units with input and output channel numbers of C_i and C_o ; **split** and **concat**: channel-wise splitting and concatenating;

Output: $\{g_j^2\}_{j=1}^G$: the feature set for generating the modulation vector ω ; $\{g_j^3\}_{j=1}^G$: the feature set used to be modulated and generate the final output of the RGPU;

```

1 for  $i \leftarrow 1, G$  do
2   if  $i = 1$  then                               /* Group 1 */
3      $f \leftarrow \text{CBR}_{3C \times C}^i(g_i)$ ;
4      $g_i^1, g_i^2, g_i^3 \leftarrow \text{split}(f)$ ;
5      $g_{prev}^1 \leftarrow g_i^1$ ;
6   else if  $i = G$  then                           /* Group G */
7      $f \leftarrow \text{CBR}_{2C \times 2C}^i(\text{concat}(g_i, g_{prev}^1))$ ;
8      $g_i^2, g_i^3 \leftarrow \text{split}(f)$ ;
9   else                                           /* Group  $i, 1 < i < G$  */
10     $f \leftarrow \text{CBR}_{3C \times 2C}^i(\text{concat}(g_i, g_{prev}^1))$ ;
11     $g_i^1, g_i^2, g_i^3 \leftarrow \text{split}(f)$ ;
12     $g_{prev}^1 \leftarrow g_i^1$ ;
13  end
14 end

```

f_{i+1}^{RGPU} from the RGPU_{i+1} as $\hat{f}_i = f_i^{MHSIU} + \mathcal{U}(f_{i+1}^{RGPU})$.

Group-wise Iteration We adopt 1×1 convolution to extend the channel number of feature map \hat{f}_i . The features are then divided into G groups $\{g_j\}_{j=1}^G$ along the channel dimension. Feature interaction between groups is carried out iteratively. Specifically, the first group g_1 is split into three feature sets $\{g_1^k\}_{k=1}^3$ after a convolution block. Among them, the g_1^1 is adopted for information exchange with the next group, and the other two are used for channel-wise modulation. In the j^{th} ($1 < j < G$) group, the feature g_j is concatenated with the feature g_{j-1}^1 from the previous group along the channel, followed by a convolution block and a split operation, which similarly divides this feature group into three feature sets. It is noted that the output of the group G with a similar input form to the previous groups only contains g_G^2 and g_G^3 . Such an iterative mixing strategy strives to learn the critical clues from different channels and obtain a powerful feature representation. The iteration structure of feature groups in RGPU is actually equivalent to an integrated multi-path kernel pyramid structure with partial parameter sharing. Such a design further enriches the ability to explore diverse visual cues, thereby helping to better perceive objects and refine predictions. The iteration processing is also listed in Alg. 1.

Channel-wise Modulation The features $[\{g_j^2\}_{j=1}^G]$ are concatenated and converted into the feature modulation vector ω by a small convolutional network, which is employed to weight another concatenated feature as $\tilde{f}_i = \omega \cdot [\{g_j^3\}_{j=1}^G]$.

Difference-based Conditional Computation Because the inter-frame difference can directly reflect the temporal motion cues of the camouflaged object in the video, we design the difference-aware adaptive routing mechanism to realize the video-specific inter-frame information propagation and seamlessly unify the image and video COD tasks. Specifically, the temporal shift [39, 70] operation is first applied to the features from the group-wise iteration and the channel-wise modulation. After shifting, the feature map of the starting time step

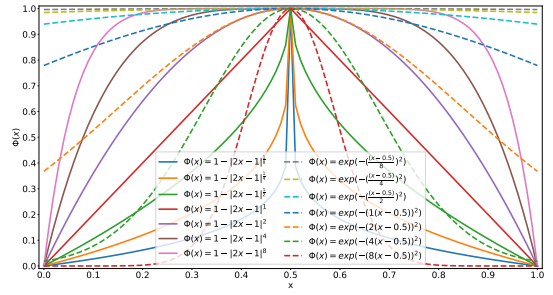


Figure 5: Curves of different forms of the proposed UAL.

in the video clip is moved to the end, while the remaining feature maps move forward by one position. Consequently, we derive the differential representation $X = \text{shift}(\tilde{f}_i) - \tilde{f}_i$ between adjacent frames. To enhance the motion cues of the object of interest between frames, the intra-frame self-attention is performed as $Z = XW_V \text{softmax}(\frac{(XW_K)^T XW_Q}{\sqrt{HW}})$. Furthermore, the following $T \times 3 \times 3$ convolutional layers are imposed to these temporal cues to realize fully connected diffusion of information inside the video clip and results are added to the original feature \tilde{f}_i . For the static image, this pipeline is not functional and outputs an all-zero tensor, thus maintaining the original static information flow. The activation of this pipeline relies on a specific input condition, *i.e.*, whether the input is sequence features with the temporal difference.

Output The output of the RGPU can be obtained by the stacked activation, normalization, and convolutional layers, which are defined as $f_i^{RGPU} = \text{fuse}(\hat{f}_i + \tilde{f}_i)$. Based on cascaded RGPUs and several stacked convolutional layers, a single-channel logits map is obtained. The final confidence map \mathbf{P} or map group $\{\mathbf{P}_t\}_{t=1}^T$ that highlights the camouflaged objects is then generated by a sigmoid function.

3.5 Loss Functions

Binary Cross Entropy Loss (BCE) The BCE loss function is widely used in various binary image segmentation tasks and its mathematical form is: $J_{BCE}^{i,j} = -\mathbf{g}_{i,j} \log \mathbf{p}_{i,j} - (1 - \mathbf{g}_{i,j}) \log(1 - \mathbf{p}_{i,j})$, where $\mathbf{g}_{i,j} \in \{0, 1\}$ and $\mathbf{p}_{i,j} \in [0, 1]$ denote the ground truth and the predicted value at position (i, j) , respectively. As shown in Fig. 8, due to the complexity of the COD data, if trained only under the BCE, the model produces serious ambiguity and uncertainty in the prediction and fails to accurately capture objects, of which both will reduce the reliability of COD.

Uncertainty Awareness Loss (UAL) To force the model to enhance “confidence” in decision-making and increase the penalty for fuzzy prediction, we design a strong constraint as the auxiliary of the BCE, *i.e.*, the uncertainty awareness loss (UAL). In the final probability map of the camouflaged object, the pixel value range is $[0, 1]$, where 0 means the pixel belongs to the background, and 1 means it belongs to the camouflaged object. Therefore, the closer the predicted value is to 0.5, the more uncertain the determination about the property of the pixel is. To optimize it, a direct way is to use ambiguity as the supplementary loss for these difficult samples. To this end, we first need to define the ambiguity measure of the pixel x , which maximizes at $x = 0.5$ and minimizes at $x = 0$ or $x = 1$. As a loss, the function should be smooth and continuous with only a finite number of non-differentiable

Table 1: Comparisons of different methods based on different backbones on static image COD datasets. *: Using more datasets. The best three results are highlighted in **red**, **green** and **blue**.

Model	Backbone	Input Size	Param.	CAMO					CHAMELEON					COD10K					NC4K				
				$S_m \uparrow$	$F_{\beta}^c \uparrow$	MAE \downarrow	$F_{\beta} \uparrow$	$E_m \uparrow$	$S_m \uparrow$	$F_{\beta}^c \uparrow$	MAE \downarrow	$F_{\beta} \uparrow$	$E_m \uparrow$	$S_m \uparrow$	$F_{\beta}^c \uparrow$	MAE \downarrow	$F_{\beta} \uparrow$	$E_m \uparrow$	$S_m \uparrow$	$F_{\beta}^c \uparrow$	MAE \downarrow	$F_{\beta} \uparrow$	$E_m \uparrow$
Convolutional Neural Network based Methods																							
SINet ²⁰ [14]	ResNet-50 [25]	352 × 352	48.947M	0.745	0.644	0.091	0.702	0.829	0.872	0.806	0.034	0.827	0.946	0.776	0.631	0.043	0.679	0.874	0.808	0.723	0.058	0.769	0.883
C ² FNet ²¹ [71]	ResNet-50 [25]	352 × 352	28.411M	0.796	0.719	0.080	0.762	0.864	0.888	0.828	0.032	0.844	0.946	0.813	0.686	0.036	0.723	0.900	0.838	0.762	0.049	0.794	0.904
SINetV2 ²¹ [17]	ResNet-50 [25]	352 × 352	26.976M	0.820	0.743	0.070	0.782	0.895	0.888	0.816	0.030	0.835	0.961	0.815	0.680	0.037	0.718	0.906	0.847	0.770	0.048	0.805	0.914
SegMaR ²² [34]	ResNet-50 [25]	352 × 352	56.215M	0.815	0.753	0.071	0.795	0.884	0.906	0.860	0.025	0.872	0.959	0.833	0.724	0.034	0.757	0.906	0.841	0.781	0.046	0.821	0.907
CamoFormer-R ²² [89]	ResNet-50 [25]	352 × 352	71.403M	0.817	0.752	0.067	0.792	0.885	0.898	0.847	0.025	0.867	0.956	0.838	0.724	0.029	0.753	0.930	0.855	0.788	0.042	0.821	0.914
Ours ²³	ResNet-50 [25]	352 × 352	28.458M	0.822	0.760	0.069	0.797	0.885	0.912	0.863	0.020	0.878	0.969	0.855	0.758	0.026	0.791	0.926	0.869	0.808	0.038	0.836	0.925
DGNet ²³ [32]	EfficientNet-B4 [73]	352 × 352	18.113M	0.838	0.768	0.057	0.805	0.914	0.890	0.816	0.029	0.834	0.956	0.822	0.692	0.033	0.727	0.911	0.857	0.783	0.042	0.813	0.922
Ours ²³	EfficientNet-B4 [73]	352 × 352	21.381M	0.859	0.815	0.049	0.845	0.920	0.911	0.864	0.020	0.877	0.965	0.868	0.789	0.023	0.818	0.937	0.878	0.832	0.035	0.857	0.932
Ours ²³	EfficientNet-B4 [73]	384 × 384	21.381M	0.867	0.824	0.046	0.852	0.925	0.911	0.865	0.020	0.879	0.964	0.875	0.797	0.021	0.824	0.941	0.884	0.837	0.032	0.862	0.939
SLSR ²¹ [48]	ResNet-50 [25]	480 × 480	50.935M	0.787	0.696	0.080	0.744	0.854	0.890	0.822	0.030	0.841	0.948	0.804	0.673	0.037	0.715	0.892	0.840	0.765	0.048	0.804	0.907
MGL-R ²¹ [90]	ResNet-50 [25]	473 × 473	63.595M	0.775	0.673	0.088	0.726	0.842	0.893	0.812	0.030	0.834	0.941	0.814	0.666	0.035	0.710	0.890	0.833	0.739	0.053	0.782	0.893
PFNNet ²¹ [50]	ResNet-50 [25]	416 × 416	46.498M	0.782	0.695	0.085	0.746	0.855	0.882	0.810	0.033	0.828	0.945	0.800	0.660	0.040	0.701	0.890	0.829	0.745	0.053	0.784	0.898
UJSC ²¹ [37]	ResNet-50 [25]	480 × 480	217.982M	0.800	0.728	0.073	0.772	0.873	0.891	0.833	0.030	0.848	0.955	0.809	0.684	0.035	0.721	0.891	0.842	0.771	0.046	0.806	0.907
ZOCTR ²¹ [88]	ResNet-50 [25]	473 × 473	48.868M	0.784	0.684	0.086	0.735	0.851	0.887	0.794	0.031	0.819	0.940	0.817	0.666	0.036	0.711	0.890	0.839	0.746	0.052	0.787	0.899
UomNet ²² [56]	ResNet-50 [25]	384 × 384	32.382M	0.820	0.752	0.066	0.794	0.892	0.902	0.845	0.023	0.864	0.958	0.838	0.729	0.029	0.766	0.911	0.853	0.784	0.043	0.818	0.912
BSA-Net ²² [102]	ResNet-50 [25]	384 × 384	32.585M	0.794	0.717	0.079	0.763	0.867	0.895	0.841	0.027	0.858	0.957	0.818	0.699	0.034	0.738	0.901	0.842	0.771	0.048	0.808	0.907
BGNet ²² [72]	ResNet-50 [21]	416 × 416	79.853M	0.812	0.749	0.073	0.789	0.882	0.901	0.851	0.027	0.860	0.954	0.831	0.722	0.033	0.753	0.911	0.851	0.788	0.044	0.808	0.916
FEDER ²³ [23]	ResNet-50 [25]	384 × 384	44.129M	0.802	0.738	0.071	0.781	0.873	0.887	0.835	0.030	0.851	0.954	0.822	0.716	0.032	0.751	0.905	0.847	0.789	0.044	0.824	0.915
Ours ²³	ResNet-50 [25]	384 × 384	28.458M	0.833	0.774	0.065	0.813	0.891	0.908	0.858	0.021	0.874	0.963	0.861	0.768	0.026	0.801	0.925	0.874	0.816	0.037	0.846	0.928
Vision Transformer based Methods																							
CamoFormer-P ²² [89]	PVTv2-B4 [79]	352 × 352	71.403M	0.872	0.831	0.046	0.854	0.938	0.910	0.865	0.022	0.882	0.966	0.869	0.786	0.023	0.811	0.939	0.892	0.847	0.030	0.868	0.946
Ours ²³	PVTv2-B4 [79]	352 × 352	65.374M	0.893	0.862	0.040	0.881	0.949	0.929	0.894	0.018	0.906	0.977	0.895	0.825	0.018	0.845	0.954	0.899	0.859	0.029	0.879	0.949
MSCAF-Net ²³ [45]	PVTv2-B2 [79]	352 × 352	30.364M	0.873	0.828	0.046	0.852	0.937	0.912	0.865	0.022	0.876	0.970	0.865	0.775	0.024	0.798	0.936	0.887	0.838	0.032	0.860	0.942
Ours ²³	PVTv2-B2 [79]	352 × 352	28.181M	0.872	0.835	0.047	0.860	0.937	0.916	0.876	0.018	0.889	0.971	0.881	0.809	0.020	0.834	0.945	0.890	0.848	0.031	0.872	0.941
HitNet ²³ [26]	PVTv2-B2 [79]	704 × 704	25.727M	0.849	0.809	0.055	0.831	0.910	0.921	0.897	0.019	0.900	0.972	0.871	0.806	0.023	0.823	0.938	0.875	0.834	0.037	0.854	0.929
FSPNet ²³ [28]	ViT-B/16 [11]	384 × 384	274.240M	0.856	0.799	0.050	0.831	0.928	0.908	0.851	0.023	0.867	0.965	0.851	0.735	0.026	0.769	0.930	0.878	0.816	0.035	0.843	0.937
SARNet ²³ [83]	PVTv2-B3 [79]	672 × 672	47.477M	0.874	0.844	0.046	0.866	0.935	0.933	0.909	0.017	0.915	0.978	0.885	0.820	0.021	0.839	0.947	0.889	0.851	0.032	0.872	0.940
Ours ²³	PVTv2-B2 [79]	384 × 384	28.181M	0.874	0.839	0.047	0.863	0.931	0.922	0.884	0.017	0.896	0.970	0.887	0.818	0.019	0.841	0.948	0.892	0.852	0.030	0.874	0.943
Ours ²³	PVTv2-B3 [79]	384 × 384	48.056M	0.885	0.854	0.042	0.872	0.942	0.927	0.898	0.017	0.905	0.977	0.895	0.829	0.018	0.848	0.952	0.900	0.861	0.028	0.880	0.949
Ours ²³	PVTv2-B4 [79]	384 × 384	65.374M	0.888	0.859	0.040	0.878	0.943	0.925	0.897	0.016	0.906	0.973	0.898	0.838	0.017	0.857	0.955	0.900	0.865	0.028	0.884	0.949
Ours ²³	PVTv2-B5 [79]	384 × 384	84.774M	0.889	0.857	0.041	0.875	0.945	0.924	0.885	0.018	0.896	0.975	0.898	0.827	0.018	0.848	0.956	0.903	0.863	0.028	0.884	0.951

Table 2: Comparisons of different methods on video COD datasets. “T” represents the number of frames in the video clip. “T=1” is the model without temporal difference, where the dynamic routing is not activated. “T=5” is our final model for the video COD task due to its better performance. †: For simplicity, the authors’ customized CUDA operators are ignored. The best three results are highlighted in **red**, **green** and **blue**.

Model	Backbone	FPS	Param.	CAD					MoCA-Mask-TE								
				$S_m \uparrow$	$F_{\beta}^c \uparrow$	MAE \downarrow	$F_{\beta} \uparrow$	$E_m \uparrow$	mDice \uparrow	mIoU \uparrow	$S_m \uparrow$	$F_{\beta}^c \uparrow$	MAE \downarrow	$F_{\beta} \uparrow$	$E_m \uparrow$	mDice \uparrow	mIoU \uparrow
EGNet ¹⁹ [93]	ResNet-50 [25]	5.682	111.693M	0.619	0.298	0.044	0.350	0.666	0.324	0.243	0.547	0.110	0.035	0.136	0.574	0.143	0.096
BASNet ¹⁹ [61]	ResNet-50 [25]	37.361	87.060M	0.639	0.349	0.054	0.394	0.773	0.393	0.293	0.561	0.154	0.042	0.173	0.598	0.190	0.137
CPD ¹⁹ [82]	ResNet-50 [25]	43.710	47.851M	0.622	0.289	0.049	0.357	0.667	0.330	0.239	0.561	0.121	0.041	0.152	0.613	0.162	0.113
PraNet ²⁰ [15]	ResNet-50 [25]	41.886	32.547M	0.629	0.352	0.042	0.397	0.763	0.378	0.290	0.614	0.266	0.030	0.296	0.674	0.311	0.234
SINet ²⁰ [14]	ResNet-50 [25]	56.509	48.947M	0.636	0.346	0.041	0.395	0.775	0.381	0.283	0.598	0.231	0.028	0.256	0.699	0.277	0.202
SINet-V2 ²¹ [17]	ResNet-50 [25]	38.307	26.976M	0.653	0.382	0.039	0.432	0.762	0.413	0.318	0.588	0.204	0.031	0.229	0.642	0.245	0.180
PNS-Net ²¹ [30]	ResNet-50 [25]	142.889	26.874M†	0.655	0.325	0.048	0.417	0.673	0.384	0.290	0.526	0.059	0.035	0.084	0.530	0.084	0.054
RRCRNet ¹⁹ [86]	ResNet-50 [25]	58.132	53.790M	0.627	0.287	0.048	0.328	0.666	0.309	0.229	0.555	0.138	0.033	0.159	0.527	0.171	0.116
MG ²¹ [87]	VGG-style CNN	272.948	4.766M	0.594	0.336	0.059	0.375	0.692	0.368	0.268	0.530	0.168	0.067	0.195	0.561	0.181	0.127
STL-Net-LT ²² [9]	PVTv2-B5 [79]	35.646	82.30														

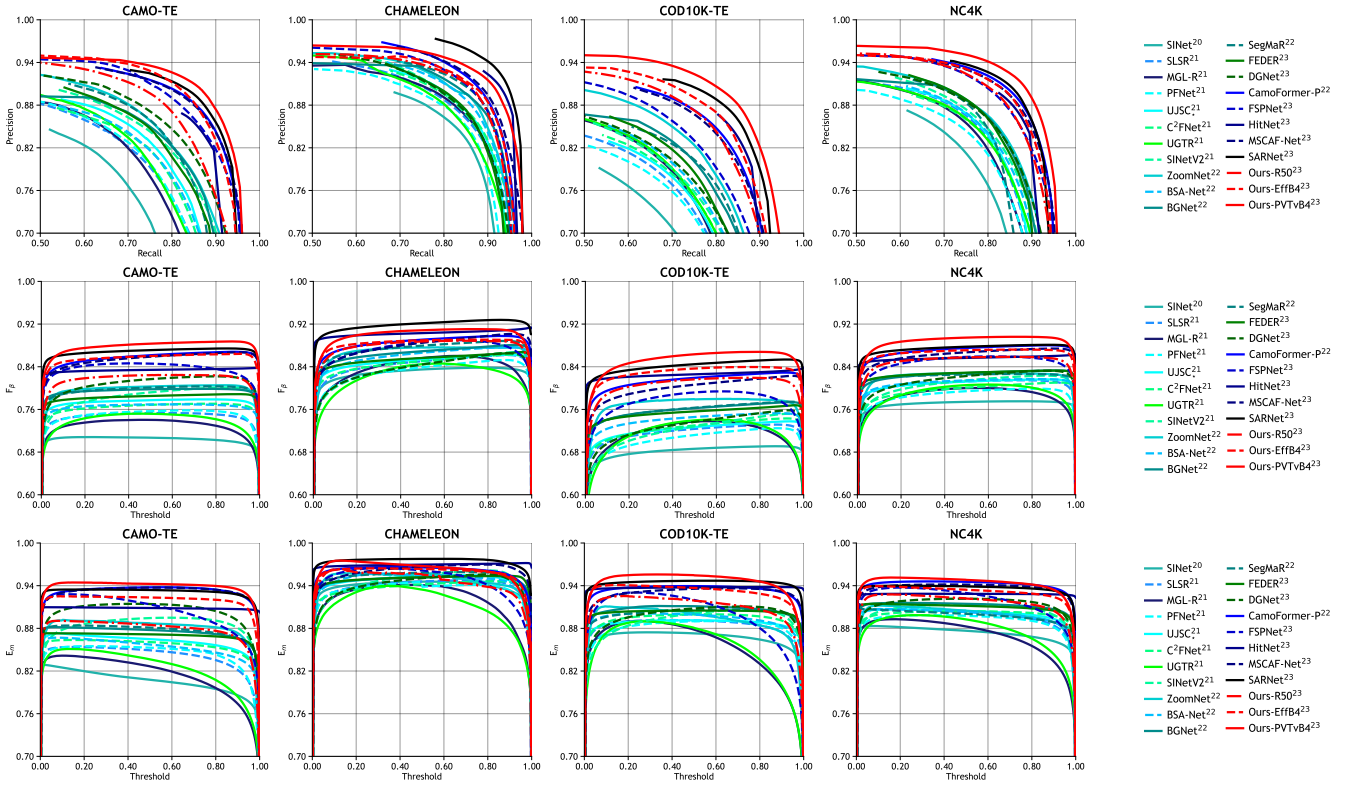


Figure 6: PR, F_β and E_m curves of the proposed model and recent SOTA algorithms over four COD datasets.

for training, and 16 sequences with 3,626 frames for testing, respectively. And it extends the original bounding box annotations of the MoCA dataset to finer segmentation annotations. The camouflaged animal dataset, *i.e.*, CAD, includes 9 short video sequences in total that accompany 181 hand-labeled masks on every 5th frame. Except for the training set containing 71 frame sequences of MoCA-Mask for training, the rest of the video sequences are used for testing as [9].

4.1.2 Evaluation Criteria

For image COD, we use eight common metrics for evaluation based on [52, 53], including S-measure [12] (S_m), weighted F-measure [49] (F_β^ω), mean absolute error (MAE), F-measure [1] (F_β), E-measure [13] (E_m), precision-recall curve (PR curve), F_β -threshold curve (F_β curve), and E_m -threshold curve (E_m curve). And for video COD, the seven metrics used in the recent pioneer work [9] are introduced to evaluate existing methods, including S_m , F_β^ω , MAE, F_β , E_m , mDice, and mIoU.

4.1.3 Implementation Details

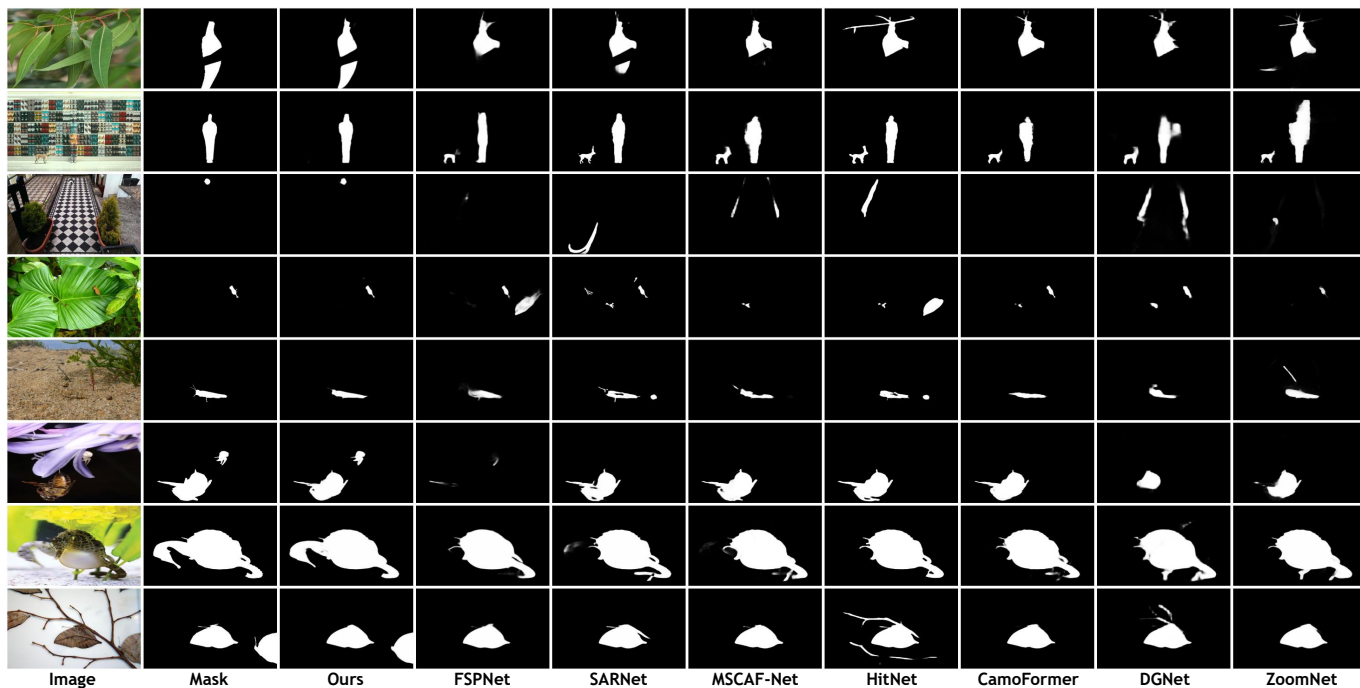
The proposed camouflaged object detector is implemented with PyTorch [57]. And the training settings are on par with recent best practices [9, 14, 32, 50, 56, 89]. The encoder is initialized with the parameters of ResNet [25], EfficientNet [73] and PVTv2 [79] pretrained on ImageNet, and the remaining parts are randomly initialized. The optimizer Adam with betas = (0.9, 0.999) is chosen to update the model parameters. The learning rate is initialized to 0.0001 and follows a step decay strategy. The entire model is trained for 150 epochs with a batch size of 8 in an end-to-end manner on an NVIDIA 2080Ti GPU. During training, the main input $I^{1.0}$ and the ground truth G are bi-linearly interpolated to 384×384 . At inference,

$I^{1.0}$ and the prediction are interpolated to 384×384 and the size of G , respectively. Considering that some methods use a smaller resolution 352×352 , we list the results with the corresponding resolution and backbone in Tab. 1. Random flipping, rotating, and color jittering are employed to augment the training data and no test-time augmentation is used during inference. In addition, for a fair comparison, we follow the settings used in [9] in the video COD task, *i.e.*, pretraining on COD10K-TR + fine-tuning on MoCA-Mask-TR.

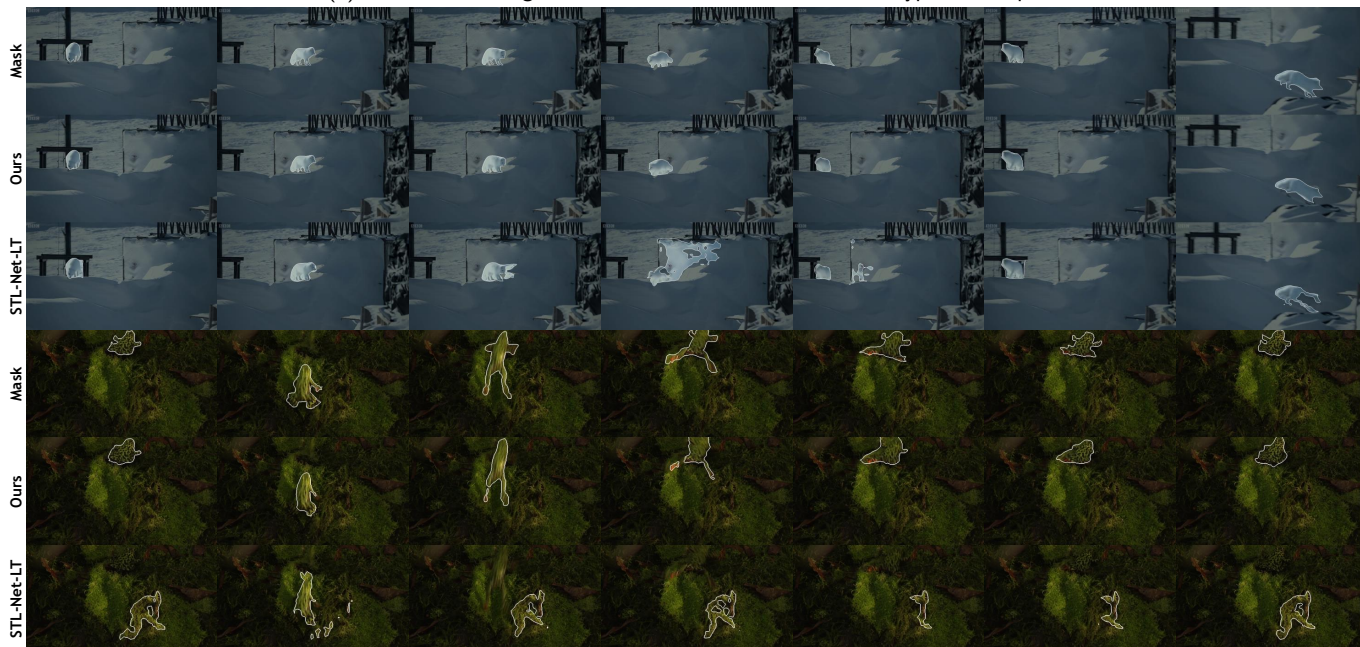
4.2 Comparisons with State-of-the-arts

In order to evaluate the proposed method, we construct a comparison of it with several recent state-of-the-art image-based and video-based methods. The results of all these methods come from existing public data or are generated by models retrained with the corresponding code. The comparison of the proposed method is summarized in Tab. 1, Tab. 2, and Fig. 6, and the qualitative performance of all methods is shown in Fig. 7a and Fig. 7b.

Quantitative Evaluation Tab. 1 and Tab. 2 show the detailed comparison results for image and video COD tasks, respectively. It can be seen that the proposed model consistently and significantly surpasses recent methods on all datasets without relying on any post-processing tricks. Compared with the recent several best methods with different backbones, ZoomNet [56], DGNet [32] and SARNet [83] for image COD and STL-Net-LT [9] for video COD, although they have suppressed other existing methods, our method still shows the obvious improvement over the conference version [56] and the performance advantages over recent methods on these datasets. Besides, PR, F_β and E_m curves marked by the red color in Fig. 6 also demonstrate the effectiveness of the proposed method. The flatness of the F_β and E_m curves reflects the consistency and uniformity of the pre-



(a) Some recent image COD methods and ours on different types of samples.



(b) “Ours (T=5)” and recent best STL-Net-LT [9] for video COD. For better visualization, grey-scale predictions are thresholded by 0.5 here.

Figure 7: Visual comparisons of image and video COD methods.

diction. Our curves are almost horizontal, which can be attributed to the effect of the proposed UAL. It drives the predictions to be more polarized and reduces the ambiguity.

Qualitative Evaluation Visual comparisons of different methods on several typical samples are shown in Fig. 7a and Fig. 7b. They present the complexity in different aspects, such as small objects (Row 3-5), middle objects (Row 1 and 2), big objects (Row 6-8), occlusions (Row 1 and 6), background interference (Row 1-3 and 6-8), and indefinable boundaries (Row 2, 3, and 5) in Fig. 7a, and motion blur in Fig. 7b. These results intuitively show the superior performance of the proposed method. In addition, it can be noticed that our predictions have clearer and more complete object regions, sharper contours, and better temporal consistency.

4.3 Ablation Studies

In this section, we perform comprehensive ablation analyses on different components. Because COD10K is the most widely-used large-scale COD dataset, and contains various objects and scenes, all subsequent ablation experiments are carried out on it.

4.3.1 Effectiveness of Proposed Modules

In the proposed model, both the MHSIU and the RGPU are very important structures. We install them one by one on the baseline model to evaluate their performance. The results are shown in Tab. 3. Note that only the inputs of the main scale are used in our baseline “0” and the models “1.x”. As can be seen, our baseline shows a good performance, probably due to the more reasonable network architecture. From the table, it can be seen that the two proposed modules make a significant contribution to

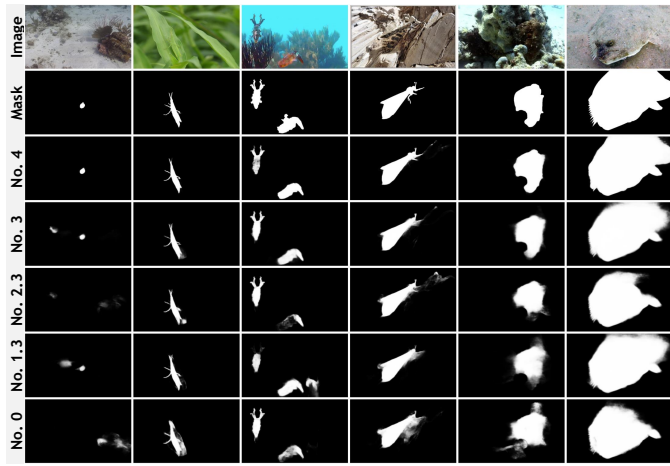


Figure 8: Visual comparisons for showing the effects of the proposed components. The names “No.*” are the same as those in Tab. 3. Please zoom in to see more details.

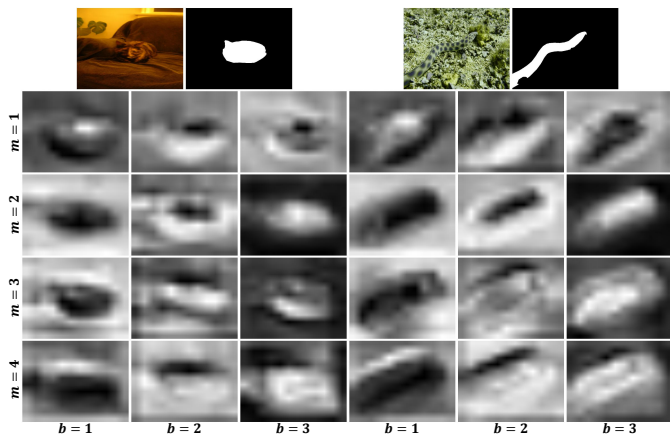


Figure 9: Spatial attention patterns from different heads $\{m = i\}_{i=1}^M$ corresponding to all branches $\{b = i\}_{i=1}^3$ in the deepest MHSIU.

the performance when compared to the baseline. Besides, the visual results in Fig. 8 show that the two modules can benefit each other and reduce their errors to locate and distinguish objects more accurately. These components effectively help the model to excavate and distill the critical and valuable semantics and improve the capability of distinguishing hard objects. Under the cooperation between the proposed modules and the proposed loss function, ZoomNeXt can completely capture the camouflaged objects of different scales and generate the predictions with higher consistency.

4.3.2 Groups in RGPU and Heads in MHSIU

RGPU The recursive iteration strategy in the proposed RGPU stimulates the potential semantic diversity of feature representation. The results in Tab. 3 show the impact of different number of iteration groups on performance. *Although increasing the number of groups introduces more parameters and computation, the performance does not keep increasing.* It can be seen from the results that the best performance appears when the number of groups is equal to 6 and also achieves a good balance between performance and efficiency. So we use 6 groups as the default setting in all RGPUs. Besides, we also replace the RGPU with the Res2Net [21] block while ensuring consistent parameters

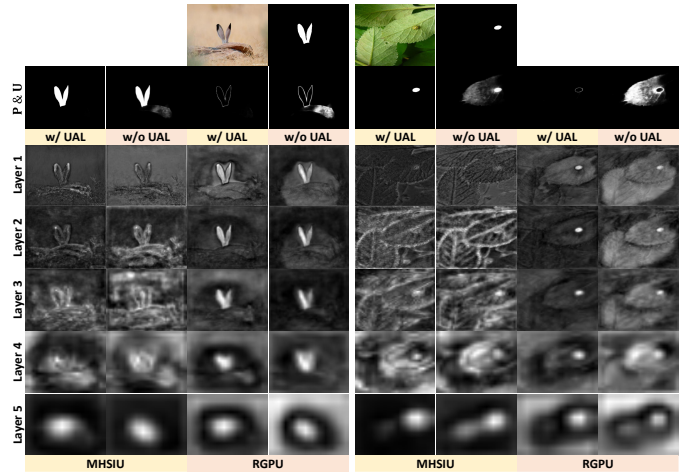


Figure 10: Intermediate feature maps from different stages of the scale merging subnetwork and the hierarchical difference propagation decoder for showing the effects of the proposed components. **P**: Prediction of the model; **U**: Uncertainty map generated by $\Phi_{pow}^2(x)$ as stated in Sec. 4.3.5.

and computations. As seen from the results in Tab. 3, our RGPU exhibits better performance. This can be attributed to the group-adaptive channel-wise modulation, which provides more efficient information modeling.

MHSIU As shown in Fig. 9, the multi-head paradigm of the MHSIU further enriches the spatial pattern of attention to fine-grained information in different scale spaces. We list the efficiency and performance of different settings in Tab. 3. The comparison shows that an increase in the number of heads improves computing efficiency and even performance. The best performance appears when the number of heads is 4, which is also the choice in other experiments.

The above experiments reflect from the side that the increase of model complexity does not necessarily lead to the improvement of performance, which also depends on more reasonable structural designs.

4.3.3 Temporal Conditional Computation

Number of Frames Our model introduces the temporal conditional computation, *i.e.*, difference-aware adaptive routing mechanism, which unifies the feature processing pipelines of image and video tasks into the same framework. Tab. 2 shows the performance corresponding to different versions of the model on the video COD task. Since there is no difference in the time dimension when only a single frame is input, the corresponding model only uses static processing nodes. As more frames are fed, adaptively activated network nodes by differential information for the inter-frame interaction further improve the performance on video COD.

Motion Modeling In Tab. 4, we also introduce two common variants concatenated with motion features from the difference map and optical flow. Both result in an increased computational burden beyond the visual model due to obtaining motion information, and the performance drops are 15.46% and 13.41% respectively when facing camouflaged objects.

Finer-grained Operations Moreover, in Tab. 4, the performance degradation caused by removing the finer-grained operations in the temporal computation of the RGPU,

Table 3: Ablation study on image COD datasets. RGPU: Rich granularity perception unit; MHSIU: Multi-head scale integration unit; L_{UAL} : Uncertainty awareness loss; ARG: Average relative gain; —: Unable to converge.

No.	Model	Param. (M)	GFLOPs	COD10K						NC4K						Δ
				$S_m \uparrow$	$F_\beta^w \uparrow$	MAE \downarrow	$F_\beta \downarrow$	$E_m \uparrow$	$S_m \uparrow$	$F_\beta^w \uparrow$	MAE \downarrow	$F_\beta \downarrow$	$E_m \uparrow$			
0	Baseline	25.216	41.000	0.826	0.677	0.035	0.724	0.903	0.850	0.756	0.049	0.800	0.912	0.00%		
1.1	No.0 + RGPU (G = 2)	25.583	47.801	0.836	0.691	0.033	0.739	0.913	0.859	0.769	0.047	0.808	0.916	\uparrow 3.05%		
1.2	No.0 + RGPU (G = 4)	26.364	62.748	0.839	0.696	0.032	0.740	0.915	0.859	0.770	0.046	0.809	0.916	\uparrow 2.71%		
1.3	No.0 + RGPU (G = 6)	27.145	77.694	0.843	0.705	0.031	0.749	0.914	0.863	0.778	0.045	0.816	0.919	\uparrow 3.77%		
1.4	No.0 + RGPU (G = 8)	27.926	92.641	0.839	0.700	0.032	0.744	0.911	0.861	0.775	0.045	0.812	0.915	\uparrow 3.10%		
1.5	No.0 + Res2Net Block	27.248	80.936	0.833	0.685	0.033	0.732	0.910	0.854	0.761	0.048	0.801	0.913	\uparrow 1.30%		
2.1	No.0 + SIU	26.762	152.720	0.852	0.721	0.031	0.763	0.919	0.862	0.780	0.044	0.818	0.919	\uparrow 4.20%		
2.2	No.0 + MH-SIU (M = 2)	26.576	150.306	0.853	0.724	0.030	0.768	0.922	0.864	0.784	0.043	0.822	0.922	\uparrow 5.41%		
2.3	No.0 + MH-SIU (M = 4)	26.530	149.100	0.856	0.728	0.029	0.770	0.923	0.870	0.789	0.043	0.825	0.924	\uparrow 6.03%		
2.4	No.0 + MH-SIU (M = 8)	26.518	148.498	0.856	0.726	0.029	0.769	0.924	0.867	0.783	0.044	0.820	0.922	\uparrow 5.59%		
3	No.0 + RGPU (G = 6) + MHSIU (M = 4)	28.458	185.794	0.861	0.734	0.029	0.773	0.924	0.875	0.792	0.042	0.826	0.925	\uparrow 6.56%		
4	No.3 + L_{UAL}	28.458	185.794	0.861	0.768	0.026	0.801	0.925	0.874	0.816	0.037	0.846	0.928	\uparrow 9.94%		
4.1	No.3 + L_{ADB} [100]	28.458	185.794	0.855	0.752	0.027	0.787	0.923	0.869	0.803	0.040	0.836	0.926	\uparrow 8.12%		
4.2	No.3 + L_{CSD} [99]	28.458	185.794	0.854	0.757	0.028	0.789	0.923	0.865	0.802	0.040	0.835	0.925	\uparrow 7.84%		
4.3	No.3 + L_{BTM} [99]	28.458	185.794	—	—	—	—	—	—	—	—	—	—	—		
4.4	No.3 + L_{MS} [99]	28.458	185.794	0.861	0.739	0.028	0.778	0.923	0.870	0.790	0.042	0.825	0.923	\uparrow 6.85%		
4.5	No.3 + L_{CSD} + L_{BTM} + L_{MS} [99]	28.458	185.794	—	—	—	—	—	—	—	—	—	—	—		

Table 4: Ablation study on video COD datasets. “w/ difference image” and “w/ optical flow”: Using the difference image and optical flow to introduce the motion cues and replace the our temporal components. “w/o intra-frame self-attention”, “w/o cross-frame cues diffusion”, and “w/o temporal shifting”: Removing the corresponding operation in the RGPU, where “w/o temporal shifting” invalidates the conditional temporal modeling capability of our method.

Model	CAD						MoCA-Mask-TE						ARG		
	$S_m \uparrow$	$F_\beta^w \uparrow$	MAE \downarrow	$F_\beta \uparrow$	$E_m \uparrow$	mDice \uparrow	mIoU \uparrow	$S_m \uparrow$	$F_\beta^w \uparrow$	MAE \downarrow	$F_\beta \uparrow$	$E_m \uparrow$		mDice \uparrow	mIoU \uparrow
Ours ²³	0.757	0.593	0.020	0.631	0.865	0.599	0.510	0.734	0.476	0.010	0.497	0.736	0.497	0.422	0.00%
w/ difference image	0.724	0.528	0.023	0.569	0.761	0.526	0.441	0.693	0.401	0.017	0.429	0.704	0.425	0.360	\downarrow 15.46%
w/ optical flow	0.729	0.534	0.022	0.573	0.765	0.532	0.450	0.697	0.409	0.016	0.436	0.708	0.433	0.370	\downarrow 13.41%
w/o intra-frame self-attention	0.741	0.552	0.023	0.588	0.862	0.574	0.490	0.683	0.394	0.013	0.412	0.684	0.413	0.352	\downarrow 10.79%
w/o cross-frame cues diffusion	0.736	0.546	0.024	0.584	0.860	0.569	0.481	0.679	0.384	0.013	0.404	0.681	0.405	0.340	\downarrow 12.17%
w/o temporal shifting	0.742	0.571	0.021	0.610	0.828	0.576	0.488	0.690	0.408	0.013	0.426	0.692	0.427	0.366	\downarrow 8.88%

further validates the important role they each play. Note that if removing the key shift operation in the temporal conditional computation, not only the overall performance will degrade, but also the temporal bypass will lose its dynamics.

4.3.4 Mixed-scale Input Scheme

Mixed Scales Our model is designed to mimic the behavior of “zooming in and out”. The feature expression is enriched by combining the scale-specific information from different scales. In Fig. 10, the intermediate features from the deep MHSIU modules show that our mixed-scale scheme plays a positive and important role in locating the camouflaged object. To analyze the role of different scales, we summarize the performance of different combination forms in Tab. 5. Our scheme performs better than the single-scale one and simply mixed one. And it also surpasses the single-scale form integrating three $1.5\times$ scales in the accuracy and efficiency, which reflects that multi-scale cues are key to the value of MHSIU. This verifies the rationality of such a design for the COD task.

Down-sampling In the MHSIU, we down-sample the high-resolution feature $f_i^{1.5}$ to supplement effective and diverse responses for camouflaged objects to $f_i^{1.0}$. To select a suitable down-sampling method, we analyze several common techniques in Tab. 6, including average-pooling, max-pooling, bi-linear interpolation, and bi-cubic interpolation. As can be seen from Tab. 6, ours based on max-pooling and average-pooling achieves better performance. So this setting is used by default in our framework.

4.3.5 Forms of Loss Function

Options of Setting λ We compare three strategies and the results are listed in Tab. 7, in which the increasing cosine strategy achieves the best performance. This may be due to the advantage of its smooth change process. This smooth intensity warm-up strategy of UAL motivates the model to take advantage of UAL in improving the learning process and to mitigate the possible negative interference of UAL on BCE due to the lower accuracy of the model during the early stage of training.

Forms of UAL Different forms of UAL are listed in Tab. 8 and the corresponding curves are illustrated in Fig. 5. As can be seen, Form 1.5 has a more balanced performance. Also, it is worth noting that, when Δ approaches 1, the form, which can maintain a larger gradient, will obtain better performance in terms of F_β^w , MAE, and F_β .

Gradient of Loss Further, from the gradient of the loss function illustrated in Fig. 11, there is a good collaboration between the proposed UAL and BCE. In the early training phase, the UAL is suppressed and the gradient is dominated by the BCE, thus facilitating a more stable optimization. However, in the later stage, the gradient of UAL is inversely proportional to Δ representing the certainty of the prediction. Such a design enables UAL to speed up updating simple samples. At the same time, it does not rashly adjust difficult samples, because they need more guidance from the ground truth.

4.3.6 Effectiveness of UAL

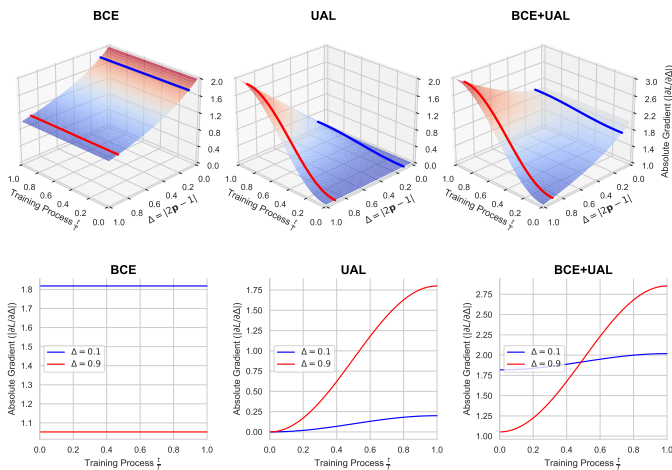
We also introduce some recent GT-free losses including L_{ADB} [100], L_{CSD} [99], L_{BTM} [99], and L_{MS} [99] in Tab. 3. Unfortunately, some of them (*i.e.*, L_{BTM} and the combined version $L_{CSD} + L_{BTM} + L_{MS}$) fail to converge due to differences in applicable scenarios and training set-

Table 5: Comparisons of mixed and single scale input schemes. All models are based on the baseline model in Tab. 3.

Input Scale	Strategy	Param. (M)	GFLOPs	COD10K					NC4K					ARG
				$S_m \uparrow$	$F_{\beta}^w \uparrow$	MAE \downarrow	$F_{\beta} \uparrow$	$E_m \uparrow$	$S_m \uparrow$	$F_{\beta}^w \uparrow$	MAE \downarrow	$F_{\beta} \uparrow$	$E_m \uparrow$	
1.0 \times	—	25.216	41.000	0.826	0.677	0.035	0.724	0.903	0.850	0.756	0.049	0.800	0.912	0.00%
0.5 \times	—	25.216	41.369	0.761	0.552	0.049	0.611	0.860	0.810	0.686	0.061	0.737	0.882	\downarrow 13.63%
0.5 \times , 1.0 \times	Addition	25.216	48.987	0.827	0.672	0.034	0.722	0.910	0.858	0.765	0.046	0.805	0.918	\uparrow 1.23%
0.5 \times , 1.0 \times	MHSIU	25.952	61.581	0.833	0.689	0.033	0.735	0.911	0.857	0.768	0.046	0.808	0.916	\uparrow 2.07%
1.5 \times	—	25.216	104.972	0.850	0.717	0.031	0.764	0.921	0.856	0.769	0.048	0.810	0.913	\uparrow 3.36%
0.5 \times , 1.5 \times	Addition	25.216	120.565	0.843	0.715	0.032	0.760	0.920	0.858	0.770	0.047	0.812	0.918	\uparrow 3.21%
0.5 \times , 1.5 \times	MHSIU	26.137	141.342	0.853	0.719	0.031	0.763	0.922	0.862	0.774	0.046	0.814	0.918	\uparrow 4.07%
1.0 \times , 1.5 \times	Addition	25.216	112.589	0.852	0.717	0.031	0.761	0.924	0.864	0.776	0.046	0.814	0.919	\uparrow 4.09%
1.0 \times , 1.5 \times	MHSIU	25.952	132.459	0.856	0.722	0.030	0.767	0.927	0.866	0.780	0.045	0.819	0.920	\uparrow 4.96%
0.5 \times , 1.0 \times , 1.5 \times	Addition	25.216	120.571	0.849	0.719	0.030	0.763	0.923	0.863	0.782	0.043	0.819	0.921	\uparrow 5.15%
0.5 \times , 1.0 \times , 1.5 \times	MHSIU	26.530	149.100	0.856	0.728	0.029	0.770	0.923	0.870	0.789	0.043	0.825	0.924	\uparrow 6.03%
1.5 \times , 1.5 \times , 1.5 \times	MHSIU	26.530	295.659	0.853	0.719	0.031	0.765	0.924	0.864	0.779	0.045	0.818	0.918	\uparrow 4.47%

Table 6: Comparisons of different down-sampling methods for the proposed MHSIU.

Method	COD10K-TE					NC4K					ARG
	$S_m \uparrow$	$F_{\beta}^w \uparrow$	MAE \downarrow	$F_{\beta} \uparrow$	$E_m \uparrow$	$S_m \uparrow$	$F_{\beta}^w \uparrow$	MAE \downarrow	$F_{\beta} \uparrow$	$E_m \uparrow$	
Ours	0.856	0.728	0.029	0.770	0.923	0.870	0.789	0.043	0.825	0.924	0.00%
w/ average-pooling	0.853	0.724	0.031	0.765	0.919	0.865	0.779	0.046	0.821	0.920	\downarrow 1.86%
w/ max-pooling	0.855	0.726	0.030	0.767	0.920	0.867	0.783	0.044	0.823	0.923	\downarrow 0.83%
w/ bi-linear	0.852	0.722	0.031	0.764	0.914	0.862	0.775	0.047	0.818	0.920	\downarrow 2.32%
w/ bi-cubic	0.853	0.723	0.031	0.766	0.916	0.863	0.777	0.046	0.819	0.921	\downarrow 1.96%

Figure 11: Gradient landscapes (*Top*) and curves (*Bottom*) of the binary cross entropy (BCE) loss and our uncertainty awareness loss (UAL) scheduled by cosine with respect to the measure $\Delta = |2p - 1|$ as in Equ. 2 and the training progress $\frac{t}{T}$, where t and T denote the current and overall iteration steps.

tings. But overall, our L_{UAL} shows a better performance. Besides, Fig. 8 and Fig. 10 intuitively show that the UAL greatly reduces the ambiguity caused by the interference from the background. We also visualize the uncertainty measure, *i.e.*, UAL, of all results on four image COD datasets in Fig. 12. The peaks of the model “w/o UAL” are flatter and more upward, which means that there are more visually blurred/uncertain predictions. Besides, in the corresponding feature visualization in Fig. 10, there is clear background interference in “w/o UAL” due to the complex scenarios and blurred edges, which are extremely prone to yield false positive predictions. However, when UAL is introduced, it can be seen in Fig. 12 that the peaks of “w/ UAL” are sharper than the one of “w/o UAL”, that is, most pixel values approach two extremes and they have higher confidence. And the feature maps in Fig. 10 become more discriminative and present a more compact and complete response in the regions of camouflaged objects.

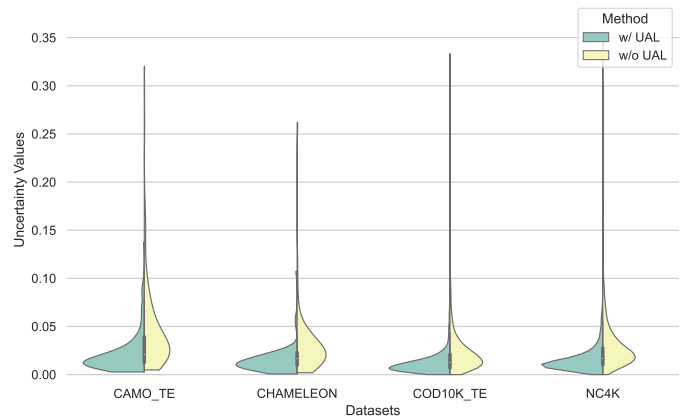


Figure 12: Visual comparison based on the violin plot for the proposed model with/without UAL. It counts the uncertainty measure of the prediction results for four image COD datasets, CAMO-TE [36], CHAMELEON [68], COD10K [14], and NC4K [48]. Better performance requires that the overall uncertainty distribution tends more toward zero. It is best to zoom in for more details.

5 Conclusion

In this paper, we propose ZoomNeXt by imitating the behavior of human beings to zoom in and out on images and videos. This process actually considers the differentiated expressions about the scene from different scales, which helps to improve the understanding and judgment of camouflaged objects. We first filter and aggregate scale-specific features through the scale merging subnetwork to enhance feature representation. Next, in the hierarchical difference propagation decoder, the strategies of grouping, mixing, and fusion further mine the mixed-scale semantics. Lastly, we introduce the uncertainty awareness loss to penalize the ambiguity of the prediction. And, to the best of our knowledge, we are the first to unify the pipelines of image and video COD into a single framework. Extensive experiments verify the effectiveness of the proposed method in both the image and video COD tasks with superior performance to existing state-of-the-art methods.

Limitations While our ZoomNeXt offers a potent and efficacious approach to the COD challenge, opportunities

Table 7: Comparisons of different increasing strategies of λ . λ_{const} : A constant value and it is set to 1. t and T : The current and total number of iterations, respectively. λ_{min} and λ_{max} : The minimum and maximum values of λ , and they are set to 0 and 1 in our experiments. “ $\star_{t_{min} \rightarrow t_{max}}$ ”: The increasing interval in the iterations is $[t_{min}, t_{max}]$, where $\lambda = \lambda_{min}$ when $t \leq t_{min}$, and $\lambda = \lambda_{max}$ when $t \geq t_{max}$.

Strategy	λ	COD10K					NC4K				
		$S_m \uparrow$	$F_\beta^\omega \uparrow$	MAE \downarrow	$F_\beta \uparrow$	$E_m \uparrow$	$S_m \uparrow$	$F_\beta^\omega \uparrow$	MAE \downarrow	$F_\beta \uparrow$	$E_m \uparrow$
Cosine $_{0 \rightarrow T}$	$\lambda_{min} + \frac{1}{2}(1 - \cos(\frac{t-t_{min}}{t_{max}-t_{min}}\pi))(\lambda_{max} - \lambda_{min})$	0.861	0.768	0.026	0.801	0.925	0.874	0.816	0.037	0.846	0.928
Cosine $_{0.3T \rightarrow 0.7T}$		0.858	0.767	0.025	0.798	0.925	0.870	0.813	0.037	0.841	0.924
Linear $_{0 \rightarrow T}$	$\lambda_{min} + \frac{t-t_{min}}{t_{max}-t_{min}}(\lambda_{max} - \lambda_{min})$	0.859	0.767	0.026	0.801	0.926	0.870	0.814	0.037	0.843	0.927
Linear $_{0.3T \rightarrow 0.7T}$		0.856	0.766	0.026	0.799	0.924	0.869	0.813	0.038	0.843	0.924
Constant	λ_{const}	0.859	0.767	0.025	0.800	0.928	0.868	0.811	0.039	0.839	0.924

Table 8: Different forms of the proposed UAL. Form 0 is our model without UAL. “—”: Unable to converge. Form 1.5 is used by default because of its balanced performance. Their curves are shown in Fig. 5.

No.	Form	ff	COD10K-TE					NC4K				
			$S_m \uparrow$	$F_\beta^\omega \uparrow$	MAE \downarrow	$F_\beta \uparrow$	$E_m \uparrow$	$S_m \uparrow$	$F_\beta^\omega \uparrow$	MAE \downarrow	$F_\beta \uparrow$	$E_m \uparrow$
0	\mathbf{x}	\mathbf{x}	0.861	0.734	0.029	0.773	0.924	0.875	0.792	0.042	0.826	0.925
1.1, 1.2, 1.3	$\Phi_{pow}^\alpha(x) = 1 - 2x - 1 ^\alpha$	1/8, 1/4, 1/2	—	—	—	—	—	—	—	—	—	—
1.4		1	0.859	0.762	0.026	0.795	0.923	0.870	0.810	0.039	0.841	0.926
1.5		2	0.861	0.768	0.026	0.801	0.925	0.874	0.816	0.037	0.846	0.928
1.6		4	0.857	0.768	0.027	0.802	0.923	0.868	0.815	0.038	0.844	0.925
1.7		8	0.859	0.767	0.026	0.802	0.924	0.867	0.814	0.038	0.843	0.923
2.1		$\Phi_{exp}^\alpha(x) = e^{-(\alpha(x-0.5))^2}$	1/8	0.866	0.741	0.027	0.782	0.933	0.875	0.794	0.041	0.828
2.2	1/4		0.862	0.736	0.028	0.777	0.928	0.876	0.794	0.041	0.828	0.926
2.3	1/2		0.863	0.742	0.028	0.781	0.930	0.876	0.798	0.040	0.831	0.927
2.4	1		0.863	0.753	0.026	0.790	0.927	0.873	0.802	0.039	0.834	0.925
2.5	2		0.862	0.762	0.026	0.797	0.927	0.873	0.810	0.038	0.841	0.928
2.6	4		0.861	0.752	0.027	0.790	0.925	0.872	0.803	0.040	0.835	0.925
2.7	8		0.861	0.737	0.028	0.778	0.929	0.874	0.793	0.041	0.827	0.926
3	BCE w/ $\omega = 1 + \Phi_{pow}^2(x)$	2	0.861	0.737	0.028	0.777	0.928	0.873	0.791	0.041	0.825	0.926

for further investigation and enhancement remain. In our current design, a shared feature extraction architecture actively gathers complementary information across a range of scales from the image pyramid, emulating the dynamic process of zooming in and out to capture detail. However, unlike our explicit approach, humans typically assimilate and internalize information effortlessly during the learning process. Despite being highly accurate for both image and video COD tasks, our scale-independent model inherently demands extra computational resources during inference.

Future Work How to further optimize the computational burden of the feature extraction component remains an important and open question. Techniques such as more compact architectural designs and scale knowledge distillation [60, 103] are directions worth exploring.

References

- [1] Radhakrishna Achanta, Sheila Hemami, Francisco Estrada, and Sabine Süsstrunk. Frequency-tuned salient region detection. In *Proc. IEEE Conf. Comput. Vis. Pattern Recognit.*, 2009. 8
- [2] Edward Adelson, Charles Anderson, James Bergen, Peter Burt, and Joan Ogden. Pyramid methods in image processing. *RCA Eng.*, 1983. 3
- [3] Yoshua Bengio. Deep learning of representations: Looking forward. In *Int. Conf. Statistical Lang. Speech Process.*, 2013. 3
- [4] Nagappa U. Bhajantri and Panduranga Naidu Nagabhushan. Camouflage defect identification: A novel approach. *Int. Conf. Inf. Technol.*, 2006. 1
- [5] Hongbo Bi, Ranwan Wu, Ziqi Liu, Huihui Zhu, Cong Zhang, and Tian-Zhu Xiang. Cross-modal hierarchical interaction network for rgb-d salient object detection. *Pattern Recognition*, 136:109194, 2023. 3
- [6] Pia Bideau and Erik Learned-Miller. It’s moving! a probabilistic model for causal motion segmentation in moving camera videos. In *Proc. Eur. Conf. Comput. Vis.* 2016. 1, 7
- [7] Ali Borji, Ming-Ming Cheng, Qibin Hou, Huaizu Jiang, and Jia Li. Salient object detection: A survey. *Comput. Vis. Media*, 2014. 3
- [8] Zhennan Chen, Rongrong Gao, Tian-Zhu Xiang, and Fan Lin. Diffusion model for camouflaged object detection. In *Eur. Conf. Artif. Intell.*, 2023. 3
- [9] Xuelian Cheng, Huan Xiong, Deng-Ping Fan, Yiran Zhong, Mehrtash Harandi, Tom Drummond, and Zongyuan Ge. Implicit motion handling for video camouflaged object detection. In *Proc. IEEE Conf. Comput. Vis. Pattern Recognit.*, 2022. 1, 3, 7, 8, 9
- [10] Bo Dong, Jialun Pei, Rongrong Gao, Tian-Zhu Xiang, Shuo Wang, and Huan Xiong. A unified query-based paradigm for camouflaged instance segmentation. In *ACM Multimedia Conf.*, 2023. 3
- [11] Alexey Dosovitskiy, Lucas Beyer, Alexander Kolesnikov, Dirk Weissenborn, Xiaohua Zhai, Thomas Unterthiner, Mostafa Dehghani, Matthias Minderer, Georg Heigold, Sylvain Gelly, Jakob Uszkoreit, and Neil Houlsby. An image is worth 16x16 words: Transformers for image recognition at scale. In *Int. Conf. Learn. Representations*, 2021. 7
- [12] Deng-Ping Fan, Ming-Ming Cheng, Yun Liu, Tao Li, and Ali Borji. Structure-measure: A new way to evaluate foreground maps. In *Proc. IEEE Int. Conf. Comput. Vis.*, 2017. 8
- [13] Deng-Ping Fan, Cheng Gong, Yang Cao, Bo Ren, Ming-Ming Cheng, and Ali Borji. Enhanced-alignment measure for binary foreground map evaluation. In *Int. Joint Conf. Artif. Intell.*, 2018. 8
- [14] Deng-Ping Fan, Ge-Peng Ji, Guolei Sun, Ming-Ming Cheng, Jianbing Shen, and Ling Shao. Camouflaged object detection. In *Proc. IEEE Conf. Comput. Vis. Pattern Recognit.*, 2020. 3, 7, 8, 12
- [15] Deng-Ping Fan, Ge-Peng Ji, Tao Zhou, Geng Chen,

- Huazhu Fu, Jianbing Shen, and Ling Shao. Planet: Parallel reverse attention network for polyp segmentation. In *Med. Image Comput. Comput. Assisted Intervention*, 2020. [1](#), [7](#)
- [16] Deng-Ping Fan, Tao Zhou, Ge-Peng Ji, Yi Zhou, Geng Chen, Huazhu Fu, Jianbing Shen, and Ling Shao. Inf-net: Automatic covid-19 lung infection segmentation from ct images. *IEEE Trans. Med. Imag.*, 2020. [1](#)
- [17] Deng-Ping Fan, Ge-Peng Ji, Ming-Ming Cheng, and Ling Shao. Concealed object detection. *IEEE Trans. Pattern Anal. Mach. Intell.*, 2021. [1](#), [3](#), [7](#)
- [18] Deng-Ping Fan, Ge-Peng Ji, Peng Xu, Ming-Ming Cheng, Christos Sakaridis, and Luc Van Gool. Advances in deep concealed scene understanding. *Vis. Intell.*, 2023. [1](#)
- [19] Clement Farabet, Camille Couprie, Laurent Najman, and Yann LeCun. Learning hierarchical features for scene labeling. *IEEE Trans. Pattern Anal. Mach. Intell.*, 2013. [3](#)
- [20] Xue Feng, Cui Guoying, Hong Richang, and Gu Jing. Camouflage texture evaluation using a saliency map. *Multimedia Systems*, 2015. [3](#)
- [21] Shang-Hua Gao, Ming-Ming Cheng, Kai Zhao, Xin-Yu Zhang, Ming-Hsuan Yang, and Philip Torr. Res2net: A new multi-scale backbone architecture. *IEEE Trans. Pattern Anal. Mach. Intell.*, 2021. [7](#), [10](#)
- [22] Hussein Hazimeh, Zhe Zhao, Aakanksha Chowdhery, Maheswaran Sathiamoorthy, Yihua Chen, Rahul Mazumder, Lichan Hong, and Ed Chi. Dselect-k: Differentiable selection in the mixture of experts with applications to multi-task learning. In *Advances Neural Inf. Process. Syst.*, 2021. [3](#)
- [23] Chunming He, Kai Li, Yachao Zhang, Longxiang Tang, Yulun Zhang, Zhenhua Guo, and Xiu Li. Camouflaged object detection with feature decomposition and edge reconstruction. In *Proc. IEEE Conf. Comput. Vis. Pattern Recognit.*, 2023. [3](#), [7](#)
- [24] Kaiming He, Xiangyu Zhang, Shaoqing Ren, and Jian Sun. Spatial pyramid pooling in deep convolutional networks for visual recognition. *IEEE Trans. Pattern Anal. Mach. Intell.*, 2015. [3](#)
- [25] Kaiming He, Xiangyu Zhang, Shaoqing Ren, and Jian Sun. Deep residual learning for image recognition. In *Proc. IEEE Conf. Comput. Vis. Pattern Recognit.*, 2016. [5](#), [7](#), [8](#)
- [26] Xiaobin Hu, Shuo Wang, Xuebin Qin, Hang Dai, Wenqi Ren, Donghao Luo, Ying Tai, and Ling Shao. High-resolution iterative feedback network for camouflaged object detection. In *AAAI Conf. Artif. Intell.*, 2023. [3](#), [7](#)
- [27] Zhou Huang, Tian-Zhu Xiang, Huai-Xin Chen, and Hang Dai. Scribble-based boundary-aware network for weakly supervised salient object detection in remote sensing images. *ISPRS-J. Photogramm. Remote Sens.*, 2022. [3](#)
- [28] Zhou Huang, Hang Dai, Tian-Zhu Xiang, Shuo Wang, Huai-Xin Chen, Jie Qin, and Huan Xiong. Feature shrinkage pyramid for camouflaged object detection with transformers. In *Proc. IEEE Conf. Comput. Vis. Pattern Recognit.*, 2023. [3](#), [7](#)
- [29] Robert A. Jacobs, Michael I. Jordan, Steven J. Nowlan, and Geoffrey E. Hinton. Adaptive mixtures of local experts. *Neural Comput.*, 1991. [3](#)
- [30] Ge-Peng Ji, Yu-Cheng Chou, Deng-Ping Fan, Geng Chen, Debesh Jha, Huazhu Fu, and Ling Shao. Progressively normalized self-attention network for video polyp segmentation. In *Med. Image Comput. Comput. Assisted Intervention*, 2021. [7](#)
- [31] Ge-Peng Ji, Guobao Xiao, Yu-Cheng Chou, Deng-Ping Fan, Kai Zhao, Geng Chen, and Luc Van Gool. Video polyp segmentation: A deep learning perspective. *Mach. Intell. Res.*, 2022. [1](#)
- [32] Ge-Peng Ji, Deng-Ping Fan, Yu-Cheng Chou, Dengxin Dai, Alexander Liniger, and Luc Van Gool. Deep gradient learning for efficient camouflaged object detection. *Mach. Intell. Res.*, 2023. [3](#), [7](#), [8](#)
- [33] Wei Ji, Ge Yan, Jingjing Li, Yongri Piao, Shunyu Yao, Miao Zhang, Li Cheng, and Huchuan Lu. Dmra: Depth-induced multi-scale recurrent attention network for rgb-d saliency detection. *IEEE Trans. Image Process.*, 2022. [3](#)
- [34] Qi Jia, Shuilian Yao, Yu Liu, Xin Fan, Risheng Liu, and Zhongxuan Luo. Segment, magnify and reiterate: Detecting camouflaged objects the hard way. In *Proc. IEEE Conf. Comput. Vis. Pattern Recognit.*, 2022. [3](#), [7](#)
- [35] Hala Lamdouar, Charig Yang, Weidi Xie, and Andrew Zisserman. Betrayed by motion: Camouflaged object discovery via motion segmentation. In *Proc. Asian Conf. Comput. Vis.* 2021. [1](#), [7](#)
- [36] Trung-Nghia Le, Tam V. Nguyen, Zhongliang Nie, Minh-Triet Tran, and Akihiro Sugimoto. Anabranch network for camouflaged object segmentation. *Comput. Vis. Image Understanding*, 2019. [3](#), [7](#), [12](#)
- [37] Aixuan Li, Jing Zhang, Yunqiu Lyu, Bowen Liu, Tong Zhang, and Yuchao Dai. Uncertainty-aware joint salient object and camouflaged object detection. In *Proc. IEEE Conf. Comput. Vis. Pattern Recognit.*, 2021. [3](#), [7](#)
- [38] Lin Li, Jingyi Liu, Shuo Wang, Xunkun Wang, and Tian-Zhu Xiang. Trichomonas vaginalis segmentation in microscope images. In *Med. Image Comput. Comput. Assisted Intervention*, pages 68–78, 2022. [1](#)
- [39] Ji Lin, Chuang Gan, and Song Han. Tsm: Temporal shift module for efficient video understanding. In *Proc. IEEE Int. Conf. Comput. Vis.*, 2019. [6](#)
- [40] Tsung-Yi Lin, Piotr Dollár, Ross Girshick, Kaiming He, Bharath Hariharan, and Serge Belongie. Feature pyramid networks for object detection. In *Proc. IEEE Conf. Comput. Vis. Pattern Recognit.*, 2017. [3](#)
- [41] Tony Lindeberg. *Scale-space theory in computer vision*. Springer Science & Business Media, 1994. [2](#)
- [42] Tony Lindeberg. Feature detection with automatic scale selection. *Int. J. Comput. Vis.*, 1998. [2](#)
- [43] Jiang-Jiang Liu, Qibin Hou, Ming-Ming Cheng, Jiashi Feng, and Jianmin Jiang. A simple pooling-based design for real-time salient object detection. In *Proc. IEEE Conf. Comput. Vis. Pattern Recognit.*, 2019. [3](#)
- [44] Liu Liu, Rujing Wang, Chengjun Xie, Po Yang, Fangyuan Wang, Sud Sudirman, and Wancai Liu. Pestnet: An end-to-end deep learning approach for large-scale multi-class pest detection and classification. *IEEE Access*, 2019. [1](#)
- [45] Yu Liu, Haihang Li, Juan Cheng, and Xun Chen. Mscafnet: A general framework for camouflaged object detection via learning multi-scale context-aware features. *IEEE Trans. Circuits Syst. Video Technol.*, 2023. [3](#), [7](#)
- [46] Jonathan Long, Evan Shelhamer, and Trevor Darrell. Fully convolutional networks for semantic segmentation. In *Proc. IEEE Conf. Comput. Vis. Pattern Recognit.*, 2015. [3](#)
- [47] Yuxuan Lou, Fuzhao Xue, Zangwei Zheng, and Yang You. Cross-token modeling with conditional computation. *ArXiv*, 2021. [3](#)
- [48] Yunqiu Lyu, Jing Zhang, Yuchao Dai, Aixuan Li, Bowen Liu, Nick Barnes, and Deng-Ping Fan. Simultaneously localize, segment and rank the camouflaged objects. In *Proc. IEEE Conf. Comput. Vis. Pattern Recognit.*, 2021. [3](#), [7](#), [12](#)
- [49] Ran Margolin, Lihi Zelnik-Manor, and Ayellet Tal. How to evaluate foreground maps? In *Proc. IEEE Conf. Comput. Vis. Pattern Recognit.*, 2014. [8](#)
- [50] Haiyang Mei, Ge-Peng Ji, Ziqi Wei, Xin Yang, Xiaopeng Wei, and Deng-Ping Fan. Camouflaged object segmentation with distraction mining. In *Proc. IEEE Conf. Comput.*

- Vis. Pattern Recognit.*, 2021. [3](#), [7](#), [8](#)
- [51] Sami Merilaita, Nicholas E. Scott-Samuel, and Innes C. Cuthill. How camouflage works. *Philos. Trans. R. Soc. B-Biol. Sci.*, 2017. [2](#)
- [52] Youwei Pang. Pysodevaltoolkit: A python-based evaluation toolbox for salient object detection and camouflaged object detection. <https://github.com/lartpang/PySODEvalToolkit>, 2020. [8](#)
- [53] Youwei Pang. Pysodmetrics: A simple and efficient implementation of sod metrics. <https://github.com/lartpang/PySODMetrics>, 2020. [8](#)
- [54] Youwei Pang, Lihe Zhang, Xiaoqi Zhao, and Huchuan Lu. Hierarchical dynamic filtering network for rgb-d salient object detection. In *Proc. Eur. Conf. Comput. Vis.*, 2020. [3](#)
- [55] Youwei Pang, Xiaoqi Zhao, Lihe Zhang, and Huchuan Lu. Multi-scale interactive network for salient object detection. In *Proc. IEEE Conf. Comput. Vis. Pattern Recognit.*, 2020. [3](#)
- [56] Youwei Pang, Xiaoqi Zhao, Tian-Zhu Xiang, Lihe Zhang, and Huchuan Lu. Zoom in and out: A mixed-scale triplet network for camouflaged object detection. In *Proc. IEEE Conf. Comput. Vis. Pattern Recognit.*, 2022. [1](#), [2](#), [5](#), [7](#), [8](#)
- [57] Adam Paszke, Sam Gross, Francisco Massa, Adam Lerer, James Bradbury, Gregory Chanan, Trevor Killeen, Zeming Lin, Natalia Gimelshein, Luca Antiga, Alban Desmaison, Andreas Köpf, Edward Yang, Zach DeVito, Martin Raison, Alykhan Tejani, Sasank Chilamkurthy, Benoit Steiner, Lu Fang, Junjie Bai, and Soumith Chintala. Pytorch: An imperative style, high-performance deep learning library. In *Advances Neural Inf. Process. Syst.*, 2019. [8](#)
- [58] Ricardo Pérez-de la Fuente, Xavier Delclòs, Enrique Peñalver, Mariela Speranza, Jacek Wierzbos, Carmen Ascaso, and Michael S Engel. Early evolution and ecology of camouflage in insects. *Proc. Nat. Acad. Sci.*, 2012. [1](#)
- [59] Thomas W. Pike. Quantifying camouflage and conspicuousness using visual salience. *Methods in Ecology and Evolution*, 2018. [3](#)
- [60] Lu Qi, Jason Kuen, Jiuxiang Gu, Zhe L. Lin, Yi Wang, Yukang Chen, Yanwei Li, and Jiaya Jia. Multi-scale aligned distillation for low-resolution detection. *Proc. IEEE Conf. Comput. Vis. Pattern Recognit.*, 2021. [13](#)
- [61] Xuebin Qin, Zichen Zhang, Chenyang Huang, Chao Gao, Masood Dehghan, and Martin Jagersand. Basnet: Boundary-aware salient object detection. In *Proc. IEEE Conf. Comput. Vis. Pattern Recognit.*, 2019. [7](#)
- [62] Shaoqing Ren, Kaiming He, Ross Girshick, and Jian Sun. Faster r-cnn: towards real-time object detection with region proposal networks. *IEEE Trans. Pattern Anal. Mach. Intell.*, 2016. [3](#)
- [63] Carlos Riquelme, Joan Puigcerver, Basil Mustafa, Maxim Neumann, Rodolphe Jenatton, André Susano Pinto, Daniel Keysers, and Neil Houlsby. Scaling vision with sparse mixture of experts. *ArXiv*, 2021. [3](#)
- [64] Matteo Rizzo, Matteo Marcuzzo, Alessandro Zangari, Andrea Gasparetto, and Andrea Albarelli. Fruit ripeness classification: A survey. *Artif. Intell. in Agriculture*, 2023. [1](#)
- [65] Olaf Ronneberger, Philipp Fischer, and Thomas Brox. U-net: Convolutional networks for biomedical image segmentation. In *Med. Image Comput. Comput. Assisted Intervention*, 2015. [3](#)
- [66] Noam M. Shazeer, Azalia Mirhoseini, Krzysztof Maziarz, Andy Davis, Quoc V. Le, Geoffrey E. Hinton, and Jeff Dean. Outrageously large neural networks: The sparsely-gated mixture-of-experts layer. *ArXiv*, 2017. [3](#)
- [67] Sheng Shen, Zhewei Yao, Chunyuan Li, Trevor Darrell, Kurt Keutzer, and Yuxiong He. Scaling vision-language models with sparse mixture of experts. *ArXiv*, 2023. [3](#)
- [68] Przemysław Skurowski, Hassan Abdulameer, Jakub Błaszczyk, Tomasz Depta, Adam Kornacki, and Przemysław Koziół. Animal camouflage analysis: Chameleon database, 2017. <http://kgwisc.aei.polsl.pl/index.php/pl/dataset/63-animal-camouflage-analysis>. [7](#), [12](#)
- [69] Martin Stevens and Sami Merilaita. Animal camouflage: current issues and new perspectives. *Philos. Trans. R. Soc. B-Biol. Sci.*, 2009. [2](#)
- [70] Swathikiran Sudhakaran, Sergio Escalera, and Oswald Lanz. Gate-shift networks for video action recognition. In *Proc. IEEE Conf. Comput. Vis. Pattern Recognit.*, 2020. [6](#)
- [71] Yujia Sun, Geng Chen, Tao Zhou, Yi Zhang, and Nian Liu. Context-aware cross-level fusion network for camouflaged object detection. In *Int. Joint Conf. Artif. Intell.*, 2021. [3](#), [7](#)
- [72] Yujia Sun, Shuo Wang, Chenglizhao Chen, and Tian-Zhu Xiang. Boundary-guided camouflaged object detection. In *Int. Joint Conf. Artif. Intell.*, 2022. [3](#), [7](#)
- [73] Mingxing Tan and Quoc Le. Efficientnet: Rethinking model scaling for convolutional neural networks. In *Proc. Int. Conf. Mach. Learn.*, 2019. [5](#), [7](#), [8](#)
- [74] Ariel Tankus and Yehezkel Yeshurun. Convexity-based visual camouflage breaking. *Comput. Vis. Image Understanding*, 2001. [3](#)
- [75] Tom Troscianko, Christopher P. Benton, P. George Lovell, David J. Tolhurst, and Zygmunt Pizlo. Camouflage and visual perception. *Philos. Trans. R. Soc. B-Biol. Sci.*, 2009. [2](#)
- [76] Ashish Vaswani, Noam Shazeer, Niki Parmar, Jakob Uszkoreit, Llion Jones, Aidan N. Gomez, undefinedukasz Kaiser, and Illia Polosukhin. Attention is all you need. In *Advances Neural Inf. Process. Syst.*, 2017. [5](#)
- [77] Tiantian Wang, Yongri Piao, Xiao Li, Lihe Zhang, and Huchuan Lu. Deep learning for light field saliency detection. In *Proc. IEEE Int. Conf. Comput. Vis.*, 2019. [3](#)
- [78] Wenguan Wang, Qiuxia Lai, Huazhu Fu, Jianbing Shen, Haibin Ling, and Ruigang Yang. Salient object detection in the deep learning era: An in-depth survey. *IEEE Trans. Pattern Anal. Mach. Intell.*, 2021. [3](#)
- [79] Wenhai Wang, Enze Xie, Xiang Li, Deng-Ping Fan, Kaitao Song, Ding Liang, Tong Lu, Ping Luo, and Ling Shao. Pvt v2: Improved baselines with pyramid vision transformer. *Comput. Vis. Media*, 2022. [5](#), [7](#), [8](#)
- [80] A. Witkin. Scale-space filtering: A new approach to multi-scale description. In *Proc. IEEE Int. Conf. Acoust. Speech Signal Process.*, 1984. [2](#)
- [81] Sanghyun Woo, Jongchan Park, Joon-Young Lee, and In So Kweon. Cbam: Convolutional block attention module. In *Proc. Eur. Conf. Comput. Vis.*, 2018. [5](#)
- [82] Zhe Wu, Li Su, and Qingming Huang. Cascaded partial decoder for fast and accurate salient object detection. In *Proc. IEEE Conf. Comput. Vis. Pattern Recognit.*, 2019. [7](#)
- [83] Haozhe Xing, Yan Wang, Xujun Wei, Hao Tang, Shuyong Gao, and Wenqiang Zhang. Go closer to see better: Camouflaged object detection via object area amplification and figure-ground conversion. *IEEE Trans. Circuits Syst. Video Technol.*, 2023. [3](#), [7](#), [8](#)
- [84] Feng Xue, Chengxi Yong, Shan Xu, Hao Dong, Yuetong Luo, and Wei Jia. Camouflage performance analysis and evaluation framework based on features fusion. *Multimedia Tools and Applications*, 2016. [3](#)
- [85] Jinnan Yan, Trung-Nghia Le, Khanh-Duy Nguyen, Minh-Triet Tran, Thanh-Toan Do, and Tam V. Nguyen. Mirror-net: Bio-inspired camouflaged object segmentation. *IEEE Access*, 2021. [3](#)
- [86] Pengxiang Yan, Guanbin Li, Yuan Xie, Zhen Li, Chuan Wang, Tianshui Chen, and Liang Lin. Semi-supervised

- video salient object detection using pseudo-labels. 2019. 7
- [87] Charig Yang, Hala Lamdouar, Erika Lu, Andrew Zisserman, and Weidi Xie. Self-supervised video object segmentation by motion grouping. In *Proc. IEEE Int. Conf. Comput. Vis.*, 2021. 7
- [88] Fan Yang, Qiang Zhai, Xin Li, Rui Huang, Ao Luo, Hong Cheng, and Deng-Ping Fan. Uncertainty-guided transformer reasoning for camouflaged object detection. In *Proc. IEEE Int. Conf. Comput. Vis.*, 2021. 3, 7
- [89] Bowen Yin, Xuying Zhang, Qibin Hou, Bo-Yuan Sun, Deng-Ping Fan, and Luc Van Gool. Camoformer: Masked separable attention for camouflaged object detection. *ArXiv*, 2022. 1, 3, 7, 8
- [90] Qiang Zhai, Xin Li, Fan Yang, Chenglizhao Chen, Hong Cheng, and Deng-Ping Fan. Mutual graph learning for camouflaged object detection. In *Proc. IEEE Conf. Comput. Vis. Pattern Recognit.*, 2021. 3, 7
- [91] Cong Zhang, Hongbo Bi, Tian-Zhu Xiang, Ranwan Wu, Jinghui Tong, and Xiufang Wang. Collaborative camouflaged object detection: A large-scale dataset and benchmark. *IEEE Trans. Neural Netw. Learn. Syst.*, 2023. 3
- [92] Yi Zhang, Jing Zhang, Wassim Hamidouche, and Olivier Deforges. Predictive uncertainty estimation for camouflaged object detection. *IEEE Trans. Image Process.*, 2023. 3
- [93] Jia-Xing Zhao, Jiang-Jiang Liu, Deng-Ping Fan, Yang Cao, Jufeng Yang, and Ming-Ming Cheng. Egnnet: Edge guidance network for salient object detection. In *Proc. IEEE Int. Conf. Comput. Vis.*, 2019. 7
- [94] Xiaoqi Zhao, Youwei Pang, Lihe Zhang, Huchuan Lu, and Lei Zhang. Suppress and balance: A simple gated network for salient object detection. In *Proc. Eur. Conf. Comput. Vis.*, 2020. 3
- [95] Xiaoqi Zhao, Lihe Zhang, Youwei Pang, Huchuan Lu, and Lei Zhang. A single stream network for robust and real-time rgb-d salient object detection. In *Proc. Eur. Conf. Comput. Vis.*, 2020. 3
- [96] Xiaoqi Zhao, Youwei Pang, Jiaying Yang, Lihe Zhang, and Huchuan Lu. Multi-source fusion and automatic predictor selection for zero-shot video object segmentation. In *ACM Multimedia Conf.*, 2021. 3
- [97] Xiaoqi Zhao, Lihe Zhang, and Huchuan Lu. Automatic polyp segmentation via multi-scale subtraction network. In *Med. Image Comput. Comput. Assisted Intervention*, 2021. 1
- [98] Xiaoqi Zhao, Youwei Pang, Lihe Zhang, Huchuan Lu, and Xiang Ruan. Self-supervised pretraining for rgb-d salient object detection. In *AAAI Conf. Artif. Intell.*, 2022. 3
- [99] Huajun Zhou, Bo Qiao, Lingxiao Yang, Jianhuang Lai, and Xiaohua Xie. Texture-guided saliency distilling for unsupervised salient object detection. *Proc. IEEE Conf. Comput. Vis. Pattern Recognit.*, 2022. 11
- [100] Huajun Zhou, Peijia Chen, Lingxiao Yang, Xiaohua Xie, and Jianhuang Lai. Activation to saliency: Forming high-quality labels for unsupervised salient object detection. *IEEE Transactions on Circuits and Systems for Video Technology*, 2023. 11
- [101] Tao Zhou, Deng-Ping Fan, Ming-Ming Cheng, Jianbing Shen, and Ling Shao. Rgb-d salient object detection: A survey. *Comput. Vis. Media*, 2021. 3
- [102] Hongwei Zhu, Peng Li, Haoran Xie, Xuefeng Yan, Dong Liang, Dapeng Chen, Mingqiang Wei, and Jing Qin. I can find you! boundary-guided separated attention network for camouflaged object detection. In *AAAI Conf. Artif. Intell.*, 2022. 3, 7
- [103] Yichen Zhu, Qiqi Zhou, Ning Liu, Zhiyuan Xu, Zhicai Ou, Xiaofeng Mou, and Jian Tang. Scalekd: Distilling scale-aware knowledge in small object detector. *Proc. IEEE Conf. Comput. Vis. Pattern Recognit.*, 2023. 13